Czech Technical University in Prague

Faculty of Electrical Engineering
Department of Control Engineering

EXPERIMENTAL LOBSTER EYE NANO-SATELLITE X-RAY TELESCOPE

Doctoral Thesis

Vladimír Tichý

Prague, November 2010

PhD. Programme: Electrical Engineering and Information Technology
Branch of study: Control Engineering and Robotics

Supervisor: Ing. Martin Hromčík, PhD.
Supervisor-Specialist: Ing. Jan Jakůbek, PhD.

Acknowledgments

X-Ray Telescope Based on Lobster Eye Optics and Pixel Detector

Mgr. Vladimír Tichý

Czech Technical University in Prague, July 2010

Supervisor: Ing. Martin Hromčík, PhD.
Supervisor-Specialist: Ing. Jan Jakůbek, PhD.

Abstract: The dissertation analyses possibility of building experimental space X-ray telescope with the optics of the lobster-eye type. This type of optics seem to be a convenient approach for building future space all-sky X-ray monitors.

Results of experiments with the lobster eye and the Medipix2 X-ray imaging device showing the functionality of this setup at the energy around 8keV are presented. Angular resolution and field of view were measured as well as image distortion and intensity in the dependency on the source position. Results are given.

Two experimental lobster eye modules called XTM-25 and XTM-90 built in Rigaku Innovative Technologies Europe, s.r.o. are presented. Results of the tests of these modules in visible light are shown. Angular resolution of these modules is described.

The lobster eye specimen called P-25 built in Rigaku Innovative Technologies Europe, s.r.o. seems to be adequate to be used in a small experimental space telescope. For this reason, performance of this lobster eye was tested in a quasi-parallel beam in Instituto Nazionale di Astrofisica-Osservatorio Astronomico di Palermo, Italy. Its key imaging parameters, i.e. field of view, angular resolution and gain were measured in several energy lines from 280eV to 8keV. At selected energy lines, measurements of gain were performed with the various incoming beam angle. Results are shown.

The simulation program was developed. The key experimental results are compared to the results of this simulation program.

Contents

List of Tables

List of Figures

Mathematical and physical symbols

c	phase velocity of electromagnetic wave in vacuum
$a \approx b$	a is approximately equal to b
$A := \ldots$	A is defined as $\ldots$
$\mathrm{int}(x)$	highest integer number less or equal than x
$\Re(z)$	real part of z
$\Im(z)$	imaginary part of z
$z^\star$	complex conjugation of z

Abbreviations

AGN	active galactic nucleus
CV	cataclysmic variable star
ESA	European Space Agency
FOV	field of view
FWHM	full width at half maximum
GRB	gamma ray burst
JAXA	Japan Aerospace Exploration Agency
KB	Kirkpatrick-Baez (type of X-ray optics)
LE	lobster eye (type of X-ray optics)
MCP	microchannel plate
NASA	National Aeronautics and Space Administration
PSPC	position sensitive proportional counter
XRB	X-ray burst

Introduction

X-rays are almost fully suppressed by Earth atmosfere and for this reason, observation of space in X-ray is possible only by the instruments placed outside the Earth atmosphere. For detailed study of space X-ray sources, X-ray imaging devices (i.e. X-ray telescopes) are necessary. In principle, X-ray telescope consists of an X-ray focussing system (X-ray optics) and an X-ray pixel detector, from this angle of view it is analogous to telescopes for visible light. However, construction of X-ray focussing systems for the astronomy is different in comparsion with systems for visible light.

At this time, several X-ray telescopes work on the Earth orbit and perform observations and measurements of the sky in X-rays. Usually, they are large systems with excellent spatial resolution, but with small field of view (1° or less). These systems allow precise measurements of selected X-ray objects.

However, also another class of X-ray telescopes is necessary. This class is called "all-sky monitors". These telescopes should perform permanent monitoring of large areas of sky and search for such type of X-ray events that are hard or impossible to predict, mainly for X-ray bursts and X-ray flashes. Also, these telescopes are necessary to perform long-term monitoring of the light curves of variable X-ray sources such as binaries, and cataclysmic variables. These monitors need not have high spatial resolution, but their key requirement is wide field of view. At this time, as the all-sky monitor for the soft X-rays, the satellite known as RXTE operates. For the focussing, this satellite uses simple devices which in principle represent one-dimensional collimators. Lobster eye concept seems to be a more advanced approach which in future can increase the sensitivity of the all-sky monitors while keeping the large field of view and the angular resolution on a moderate level.

In this thesis, the idea of the small experimental lobster telescope based on the lobster eye X-ray optics is analysed. This thesis was initiated and accomplished as a response to the strategic decision, made by the Department of Control Engineering leaders roughly five years ago, towards space oriented projects. Two driving forces can be recognized behind this initia-

tive. First, starting 2009, the Czech Republic became a full member of the European Space Agency, ESA [70]. Consequences are eminent and include direct access of Czech research teams to resources provided by ESA in dedicated calls (providing up to millions euros), and expected participation of Czech researchers and developers in ESA supported strategic projects led by ESA Primal Contractors, top European companies in space science and technology like EADS, Thales/Alenia and others. Secondly, the Department became a member of the European SpaceMaster consortium [71] in the year 2005, implementing the Joint European Master in Space Science and Technology. It is quite natural that direct access to teams like Kiruna Space Campus, Space Dynamics Lab/Utah State University, SAAB Aerospace or EADS Innovation Works, should be exploited also in the R&D sphere, going beyond purely educational nature of the SpaceMaster project.

Given no previous experience of the Department in space projects, we focused on the CubeSat[68, 69] idea and concept as a feasible direction of our research. Note that small one- to three-liters satellites are a common platform at many prestigious universities worldwide, with many published technical solutions and payload case studies, and, most important, are developed and released for decades also at two SpaceMaster partner institutions (University of Wuerzburg, Utah State University). Obviously, one way to explore was to get involved in such running projects. More specifically, our intention was to identify running particular CubeSat technology projects, provide our knowledge and skills, and develop in cooperation crucial technical solutions like orientation sensing and actuation that could be later used at a prospective CTU own CubeSat.

As we had significnt previous experience with X-ray imagers, X-ray on-orbit astronomy was soon identified as the way to go regarding intended payload. We were extremely pleased to recognize and get in touch with Czech institutes and companies active in the X-ray imaging and optics field (UTEF, Rigaku atd., vyjmenovat), all of them on the top level in the world's context, who got excited about the whole idea and have been supporting it strongly all the time.

Review of the present and past X-ray missions is performed in chapter 1. Concrete goals of the disseration are named in chapter 2. Review of the X-ray optics is the topic of chapter 3. Chapter 4 describes the principle of the lobster eye in detail. Here, also physical principles are resumed. Chapter 5 gives the review of the main X-ray imaging devices with aim to the devices usable in a small X-ray telescope. In chapter 6, experimental lobster eye modules are introduced. The principles used in the simulation program are described in chapter 7. The key part of the thesis, chapter 8 shows the

results of the experiments with the lobster eye specimens. The conclusion of the dissertation is performed in chapter 9. The possible goals of the future work are outlined in chapter 10.

Many of the figures are coloured, however they are still readable in the black-and-white print. Where it is necessary (mainly in the graphs), different types of lines and marks are used to keep them recognizable in the black-and-white print.

Chapter 1

State of the art

1.1 Beginning of X-ray astronomy devices

First X-ray emissions from an extra-terrestrial source were detected in the 1949 experiment on the rocket V-2. First extra-solar X-ray source was discovered in 1962 in the experiment on the sounding rocket Aweobee, this experiment was originally proposed to study X-ray emissions of the Moon. First satellite designed specifically for X-ray astronomy, called Uhuru[76], was launched in 1970. This satellite carried proportional counters for X-ray detection without the possibility of imaging. Nevertheless, this satellite performed important discoveries, like binary X-ray sources Cen X-3 [27], Vela X-1[14] and Her X-1[30].

1.2 Related space missions with X-ray imaging instruments

The future lobster eye telescope will operate in soft X-ray energy range (energies of order of keV). This section gives a review of missions aimed to study of X-ray sources in this range using an X-ray telescope. Some missions are aimed to study on another field and they use X-ray telescope for soft X-rays as an auxiliary instrument, for example Integral, Swift, etc. These missions are not mentioned.

1.2.1 Einstein (HEAO-2)

First satellite carying an X-ray imaging device was HEAO-2, also denoted as HEAO-B, later renamed to Einstein [46], see Fig. 1.1(a). It was launched

on the 12th November 1978 by NASA. Einstein carried Wolter-I optics[34] of focal length 340cm with four exchangeable detecting instruments. At one time, at most one detecting instrument could work. Two of these instruments allowed imaging. One of the imaging detectors was the Imaging Proportional Counter (IPC). It worked in the energy range 0.4-4.0 keV with FOV 75′ and spatial resolution 1′. Second imaging instrumend was called High Resolution Imager (HRI). It worked in the energy range 0.15-3.0 keV with FOV 25′ and spatial resolution 2″. Other two instrumets were solid state spectrometer (SSS) for the energy range 0.5-4.5keV and the focal plane crystal spectrometer (FPCS) for energy range 0.42-2.6keV. The Einstein satellite realised first high resolution spectroscopy and morphological studies of supernova remnants. Scientists recognized that coronal emissions in normal stars are stronger than expected. It resolved numerous X-ray sources in the Andromeda Galaxy and the Magellanic Clouds. It provided first studies of the X-ray emitting gas in galaxies and clusters of galaxies revealing cooling inflow and cluster evolution. It detected X-ray jets from Cen A and M87 aligned with radio jets [18]. It provided first medium and Deep X-ray surveys. It discovered thousands of "serendipitous" sources [13]. Mission HEAO-2/Einstein was ended in April 1982.

1.2.2 EXOSAT (HELOS)

The satellite EXOSAT, originally called HELOS [47], see Fig. 1.1(b) was launched on 26th May 1983 by ESA. The denotation EXOSAT means European X-ray Observing SATellite. EXOSAT carried more instruments, two of them allowed imaging. Both imaging instruments were called LEIT (low-energy imaging telescopes), sometimes the shortened denotation LE is used for them. The LEIT contained Wolter-I X-ray optics and it was designed for observations in energy range 0.05-2keV. As detectors, two devices were possible to use[17]: CMA (Channel-multiplier array) and PSD (position sensitive proportional counter). The FWHM [38] resolution for on-axis sources was 24″, however it fell to 4′ for 1° off-axis source position.

The EXOSAT performed many observations of active galactic nuclei, stellar coronae, cataclysmic variables, white dwarfs, X-ray binaries, clusters of galaxies and supernova remnants [7, 33]. EXOSAT operated until 9th April 1986.

1.2.3 ROSAT

The ROSAT satellite [31, 48, 49], see Fig. 1.1(c) was a joint German, US and British X-ray astrophysics project. Its name is an abbreviation of RÖntgenSATellit

in honour of X-ray discoverer Wilhelm Röntgen. The ROSAT was launched on June 1, 1990 by a NASA rocket.

Scientific payload of ROSAT consisted of two X-ray imaging instruments [24]. Primary instrument was XRT (X-ray telescope),secondary instrument was called WFC (wide field camera).

XRT contained Wolter-I X-ray optics[2] with focal length of 240cm and field of view of $2°$. The device was designed for observations in the energy range of 0.1 to 2.4 keV. As detector, PSPC (position sensitive proportional counter) or device called HRI (high resolution camera) could be used. PSPC was intented for energy measurements, with this detector the on-axis spatial resolution was approx. $25''$. HRI allowed observations with spatial resolution of $1.7''$ FWHM.

WFC used Wolter-Schwarzchild nested mirrors of focal length 52.5cm for focussing and MCP detector for detection. WFC operated from soft X-ray energies to extreme ultraviolet region with energies of 0.04-0.2keV. Its field of fiew was $5°$ and spatial resolution was $2.3'$.

1.2.4 RXTE

The denotation RXTE means "Rossi X-ray Timing Explorer". The RXTE was launched on 30 December 1995 by NASA and it is still in operation. The RXTE carries three scientific instruments: PCA (Proportional Counter Array, HEXTE (High-Energy X-ray Timing Experiment) and ASM (All Sky Monitor). Observations are aimed mainly to black holes, neutron stars, X-ray pulsars and X-ray bursts. RXTE artists image is shown on Fig. 1.1(d), more information about satellite and mission can be found mainly on [53, 54].

The ASM is an imaging device consisting of three special X-ray focussing devices called shadow cameras, acting as an one-dimensional collimator. As detectors, xenon position sensitive proportional counters are used. The ASM operates at energies of range 2-10keV. The FOV of each of the three cameras is $6° \times 90°$, their spatial resolution is $3' \times 15'$. These parameters and the purpose of the ASM are similar to the proposed telescope with lobster eye. However, sensitivity of the ASM is only 30mCrab (unit crab represents the luminosity of the crab nebula, see [16]).

1.2.5 BeppoSAX

BeppoSAX [3, 55, 56] was an Italian-Dutch satellite launched in 30 April, 1996 by NASA. BeppoSAX was named in honour of the Italian physicist Giuseppe "Beppo" Occhialini. SAX stands for "Satellite per Astronomia

a raggi X" or "Satellite for X-ray astronomy". BeppoSAX is imaged on
Fig. 1.2(a).

BeppoSAX carried five science instruments [57]: Low Energy Concentrator Spectrometer (LECS), Medium Energy Concentrator Spectrometer (MECS), High Pressure Gas Scintillation Proportional Counter (HPGSPC), Phoswich Detector System (PDS) and Wide Field Camera (WFC). The first four instruments (often called Narrow Field Instruments or NFI) pointed to the same direction and allow observations of an object in a broad energy band of 0.1 to 300 keV.

WFC was an imaging instrument. It used coded mask and was designed for observations at energies 1.8-28keV. WFC had a large field of view of $40 \times 40°(20 \times 20°\text{FWHM})$. Spatial resolution of WFC was $5'$ and sensitivity 1mCrab (@3.10^4s). As a detector, PSPC was used. Primary objective of this instrument was survey of the galactic plane and the search of X-ray transients for follow-up studies with the narrow field instruments. Secondary objective was monitoring of faint sources, like AGN.

BeppoSAX was deorbited on 29 April 2003.

1.2.6   Chandra (AXAF)

The Chandra X-ray Observatory[58, 59, 60] represents one of the most important X-ray missions. It was launched by NASA on July 23, 1999 and operates till today. Chandra was named in honor of Indian-American physicist Subrahmanyan Chandrasekhar who is known for determining the maximum mass for white dwarfs. "Chandra" also means "moon" or "luminous" in Sanskrit. AXAF means "Advanced X-ray Astrophysics Facility", this denotation was being used before the launch. Chandra is imaged on Fig. 1.2(b). Chandra's capabilities are unprecedented and Chandra users keep making important contributions to all areas of astronomy, including the solar system, stars, interacting binaries, compact objects, supernovae, galaxies, and AGN.

Chandra carries four scientific instruments: Charged Coupled Imaging Spectrometer (ACIS), High Resolution Camera (HRC), High Energy Transmission Grating (HETG), Low Energy Transmission Grating (LETG). ACIS and HRC are X-ray imaging detectors placed in the focus of the Wolter optics with the focal length of 10.1m.

HRC consists of two similar devices: HRC-I and HRC-S. HRC-I has field of view of $30 \times 30'$, HRC-S has field of view of $6 \times 90'$. HRC-I and HRC-S represent a dual MCP detector. They operate in energies of 0.08-10keV and with the mentioned optics, they reach excellent angular resolution of $0.5''$. The HRC is especially useful for imaging hot matter in remnants of exploded stars, and in distant galaxies and clusters of galaxies, and for identifying very

faint sources. Limiting sensitivity is $9 \cdot 10^{-16} \mathrm{erg\,cm^{-2}\,s^{-1}}$ in $3 \cdot 10^5$s.

ACIS consists of 10 CCD detectors, its main purpose is to get a spectroscopic information simultaneously with an image. It operates in energies of 0.1-10keV and its angular resolution is $2''$. Four of the CCDs are arranged to an array of 2×2 detectors, denoted as ACIS-I. These CCDs are front-illuminated, they cover a field of view of $16.9 \times 16.9'$ and they serve for capturing of X-ray images. Remaining six CCDs are arranged to an array of 6×1 detectors, denoted as ACIS-S. Four of them are front-illuminated, two are back-illuminated. ACIS-S covers a field of view of $8.3 \times 50.6'$ It is being used for acquiring spectra. Limiting sensitivity of ACIS is $4 \cdot 10^{-15} \mathrm{erg\,cm^{-2}\,s^{-1}}$ in 10^4s.

HETG and LETG provide transmission gratings, which swing into the optical path behind the mirrors with high resolution spectroscopy. The HETG works over $0.4 - 10$keV, LETG has a range of $0.09 - 3$keV.

More information about Chandra scientific instruments can be found in [63].

1.2.7   XMM-Newton

XMM-Newton (X-ray Multi-Mirror Mission - Newton) [12, 64, 65, 66] is the X-ray observatory named in honor of Sir Isaac Newton. It represents one of the most important X-ray missions. XMM-Newton was launched on December 10, 1999 by ESA and it is still in operation.

XMM-Newton carries three X-ray telescopes, each of them is based on Wolter-I optics [67]. Focal length of these telescopes is 7.5meters. FWHM resolution of all systems is better than $6.6''$ in energy range of $1.5 - 8$keV.

For X-ray imaging, XMM-Newton has three devices called European Photon Imaging Camera (EPIC) [32, 28]. Two of them are called MOS-cameras [32]. They are installed behind the two X-ray optical systems and they are equipped with the gratings of the Reflection Grating Spectrometers (RGS). The gratings divert about half of the telescope incident flux towards the RGS detectors such that (taking structural obscuration into account) about 44% of the original incoming flux reaches the MOS cameras. The third EPIC is called pn-camera [28]. It is installed behind the third optics and it has an unobstructed beam.

Both types, MOS-camera and pn-camera are based on CCD-detectors, called MOS-CCD and pn-CCD respectively. The EPIC cameras offer the possibility to perform extremely sensitive imaging observations over the telescope's field of view (FOV) of $30'$ and in the energy range from 0.15 to 15 keV with angular resolution of $6''$ FWHM. RGS gives a spectroscopic information.

(a) Einstein (HEAO-2) [37]

(b) EXOSAT (HELOS) [47]

(c) ROSAT [37]

(d) RXTE [53]

Figure 1.1: Artistic views of X-ray mission satellites (1)

XMM-Newton also carries device called Optical monitor (OM) [21]. This device is designed for imaging the radiation of the wavelengths of $170-650$nm (UV and a part of visible light).

1.2.8   IXO

IXO is one of the most important planned X-ray missions. The denotation means International X-ray Observatory. It is a joint project of NASA, ESA and JAXA merging previously planned missions XEUS (X-ray Evolving Universe Spectroscopy) of ESA and Constellation-X of NASA.

Wolter-I mirror system of focal length 20m and diameter of 3m is planned to be used. For imaging, a CCD camera will be used. Other planned instrumentation consists of high-resolution spectrometers, microcalorimeter and X-ray grating spectrometer.

IXO is planned to be launched in 2021.
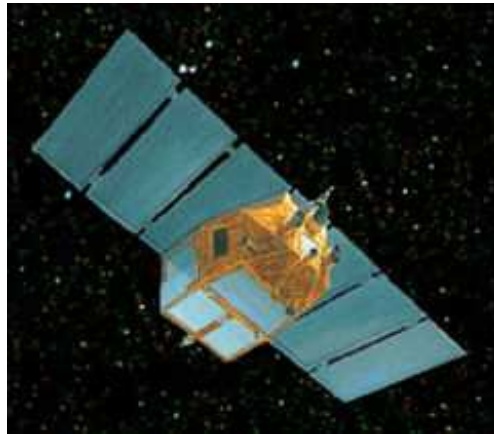
(a) BeppoSAX [56]

(b) Chandra (AXAF) [58]

(c) XMM-Newton [64]

Figure 1.2: Artistic views of X-ray mission satellites (2)

Mission	Instrument	Type of optics	Detector	Energy range [keV]	FOV size [arcmin]	Spatial resolution [arcsec]	Focal length [m]	Life years
Einstein (HEAO-2)	HRI IPC	Wolter-I (common)	MCP PSPC	0.15-3 0.4-4	25 75	2 60	3.4	1978-1981
EXOSAT (HELOS)	LEIT (2 pcs.)	Wolter-I	CMA+PSD	0.05-2	120	24-240	1.1	1983-1986
ROSAT	XRT WFC	Wolter-I Wolter-Schwarzschild	PSPC/HRI MCP	0.1-2.4 0.04-0.2	120 300	25/1.7 140	2.4 0.525	1990-1999
RXTE	ASM (3 pcs.)	shadow camera	PSPC	2-10	360×5400	180×900	-	1995-now
BeppoSAX	WFC	Coded mask	PSPC	1.8-28	2400×2400	300	1.85	1996-2003
Chandra (AXAF)	HRC-I HRC-S ACIS-I ACIS-S	Wolter-I (common)	MCP MCP CCD CCD	0.08-10 0.08-10 0.2-10 0.2-10	30×30 6×90 16.9×16.9 8.3×50.6	0.5 0.5 2 2	10.1	1999-now
XMM-Newton	EPIC (3 pcs.)	Wolter-I	CCD	0.15-15	30	6	7.5	1999-now

Table 1.1: Overview of main X-ray missions with X-ray imaging instruments

Chapter 2

Goals of the dissertation

2.1 Medipix2 and Timepix

Perform laboratory tests with Medipix2 and Timepix detectors. Assess applicability of these detectors for a small space lobster eye X-ray telescope.

2.2 Tests of lobster eye optics for X-ray imaging from finite distance

Perform basic laboratory tests of a lobster eye specimen designed for imaging from finite distance. Determine field of view and spatial resolution. Estimate image distortion as function of source position.

2.3 Experimental modules

Handle manufacturing of experimental X-ray telescope modules for both accessible lobster eyes for imaging from infinity. Perform tests of both these modules in the visible light. Estimate spatial resolution.

2.4 Tests of lobster eye optics for X-ray imaging from infinite distance

For these tests, X-ray beam of low divergence (less than 1arcmin) and relatively large beam (of diameter at least 3cm) have to be used. Because no institution in the Czech Republic operates such device, first it is necessary to establish collaboration with a suitable foreign institute.

Tests will be performed with a selected specimen of the lobster eye. Test imaging with this specimen at several energy lines. Estimate gain, spatial resolution and field of view at all these lines. At some lines, estimate gain as a function of the source position.

2.5   Simulation program

Create a program for simulation of the lobster eye operation in the centered arrangement (i.e. when the X-ray source and the detector lay in the optical axes of the lobster eye). This program should simulate behavior of any lobster eye configuration for any energy, visualize the image and estimate the gain.

2.6   Assesment

Discuss accordance between the theory and measured results. Compare results of the X-ray tests with the results of the simulations. Discuss the differences. Discuss suitability of lobster eyes for a space telescope.

Chapter 3

X-ray optics overview

3.1   Principles of X-ray optics

According to the physical processes involved, X-ray optics can be divided into the following groups:

- Pin-holes and coded appertures

- Refractive optics

- Reflective optics

- Other (Fresnel lenses, etc.)

3.2   Pin-holes and coded appertures

The construction of pin-holes and coded appertures for X-rays is similar to the construction of analogous systems for a visible light. Spatial resolution of these systems is limited by the ratio of apperture diameter and the length of the system. The efficiency of the pin-holes is very low. The efficiency can be make better by construction of coded appertures.

3.3   Refractive X-ray optics

The principle of the refractive X-ray optics is similar to the principle of the common lenses for the visible light. This type of optics provides high spatial resolution, however its efficiency is low because of high attenuation of radiation in the material of the lens. This type of optics is not suited for the astronomic applications.

3.4 Reflective X-ray optics

Reflective X-ray optics uses sets of reflecting surfaces for focusing. This optics provides high efficiency, and it is the usual type of optics for the astronomical applications in the soft X-ray range.

This type of X-ray optics use reflecting surfaces for the focusing (physical principles of X-ray reflection are described in section 4.1) There exists several different geometric arrangements of the surfaces. Their main types are being called Kirkpatrick-Baez, Wolter and Lobster Eye.

3.4.1 Wolter X-ray optics

Wolter arrangement[34] was suggested by H. Wolter in the mid 20th century. There exist three types of Wolter design. All Wolter designs consist of two reflecting surfaces. These designs are drawn on Fig. 3.1. Design Wolter I is based on reflection on a convex side of a parabola and on a convex side of a hyperbola. Design Wolter II is based on reflection on a convex side of a parabola and on a concave side of a hyperbola. Design Wolter III is based on reflection on a concave side of a parabola and on a convex side of a ellipse. Wolter X-ray optics is used in laboratory devices as well as in high-performance space X-ray telescopes. These systems have excellent angular resolution, however their FOV is small, typically 1° or less due to the limiting angle of the used material for the used X-ray energy.

3.4.2 Lobster eye X-ray optics

Lobster eye can be constructed as one-dimensional or a two-dimensional system. 1-D system [26] uses a set of flat mirrorirng surfaces. These mirrors are arranged in uniform radial pattern around the perimeter of a cylinder, see Fig. 3.2. The reflected incoming X-rays are focussed roughly to a line. Also it is seen on Fig. 3.2 that some rays can travel through this system directly, one of them is shown. Note that this figure is schematic only. In reality, spaces between mirrors are narrower and the amount of direct beams is lower than it appears on Fig. 3.2.

2-D system uses two such sets arranged orthogonaly (Schmidt design [26]) or it is based on set of chambers (Angel design [1]). Comparsion of these arrangements is seen on Fig. 3.3. Example of Schmidt type lobster eye can be seen on Fig. 3.4. Angel design is inspired by compound eyes of lobsters (Fig. 3.5, Fig. 3.6) and for this reason, this type of optics is called "lobster eye".

16
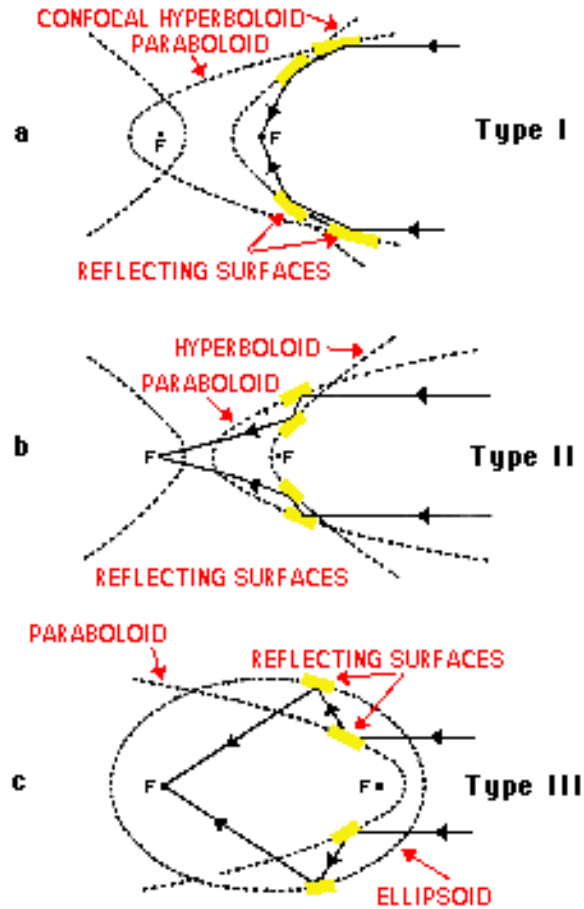
Figure 3.1: Wolter types of X-ray optics, source: [37]

Angel design of the lobster eye is the only one type of reflective X-ray optics which theoretically can cover the whole sphere by its field of view. In real cases, obtainable field of view is limited, because X-ray detectors are flat.

The main factor limiting the FOV in the Schmidt design is the distortion of the image for off-axis source position. This distortion increases with the angle between the optical axis and the source. This fact limits the applicable area to approx. $10° \times 10°$ [26].

For both designs, size of the active area of the detector can also limit the FOV. More detailed description of lobster eye X-ray optics is given in chapter 4.
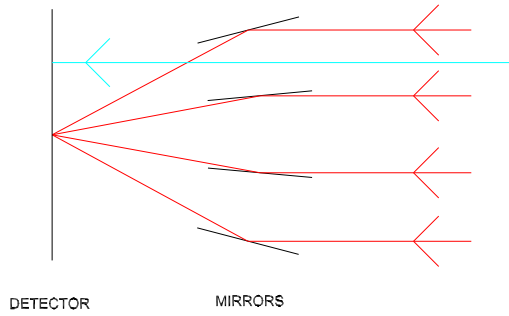
Figure 3.2: One-dimensional lobster eye principle. The rays are incomming from the right hand side and they are focussed to the detector on the left hand side. In reality, spaces between mirrors are narrower.

3.4.3 Kirkpatrick-Baez X-ray optics

Analogously to the Schmidt lobster eye, Kirkpatrick-Baez (KB) optics [15] consists of two orthogonally arranged sets of mirrors. Contrary to LE, these mirrors are not flat but specially curved. It decreases the spot size for on-axis source and the sources near the optical axis, however decreases the obtainable field of view. Its principle is drawn on Fig. 3.7, where only one mirror of each of the two sets is drawn.
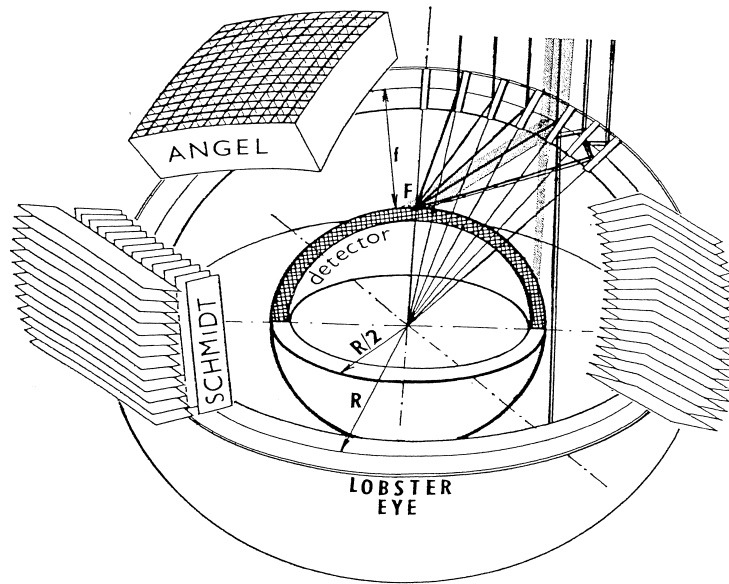
Figure 3.3: Lobster eye principle and comparsion of Schmidt and Angel lobster eyes, source: [10]. The outer sphere represents the lobster eye of the radius R. The inner sphere represents the detector. It has radius $R/2$ because focal length f of the lobster eye system is equal to $R/2$. On the top side, several rays are shown. They are focussed by outlined channels to the focus F. Around the outer sphere, Schmidt 2-D (on the left hand side), Angel (on the top side, slighly to the left) and Schmidt 1-D (on the right hand side) systems are drawn.
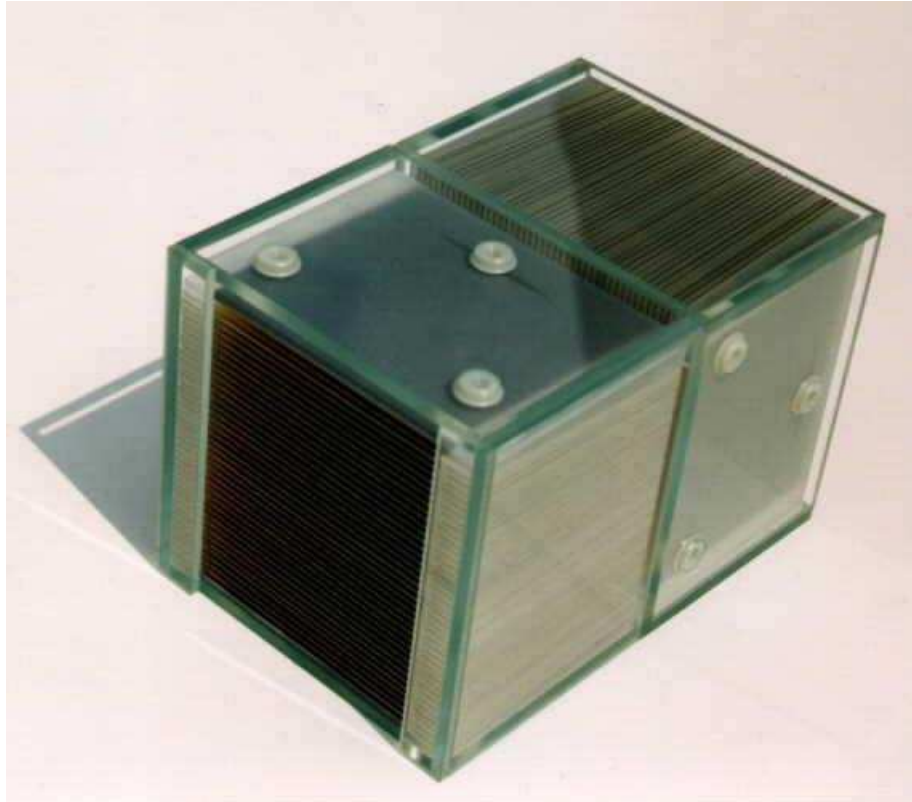
Figure 3.4: Photograph of the Schmidt type lobster eye consisting of the plates of diameter 100x80 mm, source: [42]

Figure 3.5: European lobster (Homarus gammarus), source: [37]

Figure 3.6: American lobster (Homarus americanus), source: [37]
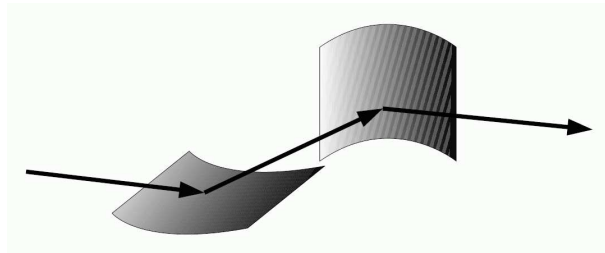
Figure 3.7: Principle of Kirkpatrick-Baez (KB) X-ray optics, source: [29]

Chapter 4

Lobster eye - mathematical description

More details on X-ray reflection and Lobster Eye optics are given in this chapter. It is supposed that reader is familiarised with chapter 3. In this chapter, LE of the Schmidt design is considered.

4.1 Physical elements of X-ray reflection

Total reflection is a known phenomenon of visible light. Also, this effect can arise for the X-ray. In general, electromagnetic beam inciding the interface between two environments is divided to reflected beam and transmitted beam, as seen on Fig. 4.1. Angles θ_I, θ_R and θ_T are called in this order incoming angle, reflecting angle and transmitting angle. These angles are measured between the ray and the normal of the surface. Angle θ_G is called grazing angle or glancing angle and it is angle between an incoming ray and a suface. Usually, a glancing angle is used instead of an incoming angle, if an incoming angle is almost equal to the right angle, i.e. if a grazing angle is small. Symbols n_1 and n_2 denote refractive indices of the environments. In general, they are complex numbers. Their real part $\Re(n)$ determines the ratio between the phase velocity of waves in the material and in the vacuum, imaginary part $\Im(n)$ determines absorption of the radiation in the material.

The intensity of the electric field of the transmitted beam is given by Fresnel equations [4]

$$\frac{E_{R\perp}}{E_{I\perp}} = \frac{n_1 \cos\theta_I - \sqrt{n_2{}^2 - n_1{}^2 \sin^2\theta_I}}{n_1 \cos\theta_I + \sqrt{n_2{}^2 - n_1{}^2 \sin^2\theta_I}} \tag{4.1}$$
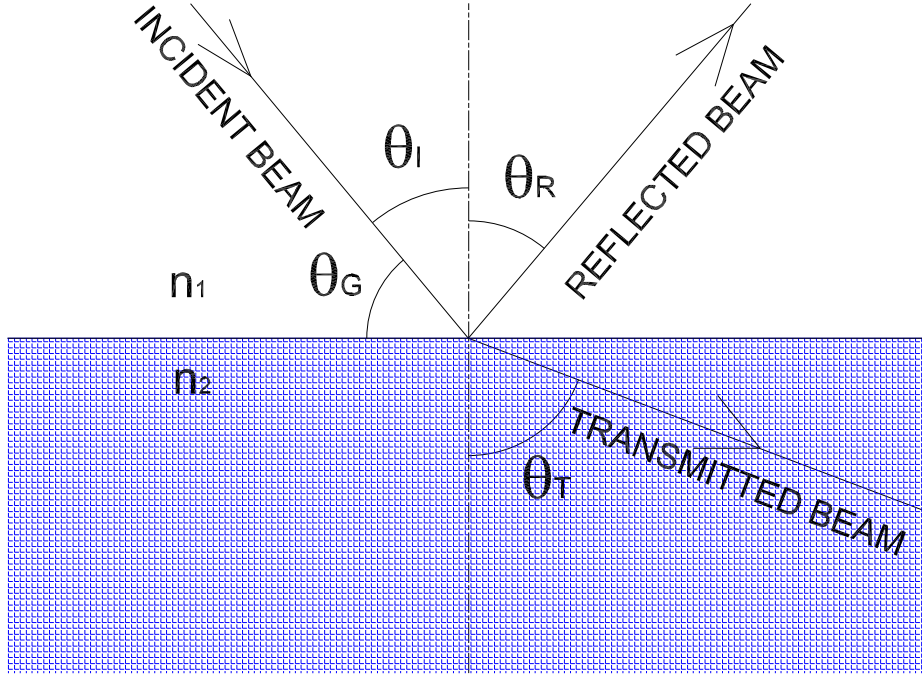
Figure 4.1: Icoming, reflected and transmitted beam

$$\frac{E_{R\parallel}}{E_{I\parallel}} = \frac{n_2{}^2 \cos\theta_I - n_1\sqrt{n_2{}^2 - n_1{}^2 \sin^2\theta_I}}{n_2{}^2 \cos\theta_I + n_1\sqrt{n_2{}^2 - n_1{}^2 \sin^2\theta_I}} \tag{4.2}$$

Here, the symbol $E_\perp$ denotes the component of vector $\vec{E}$ which is perpendicular to the surface and symbol $E_\parallel$ denotes the component which is parallel to the surface. Index $_I$ denotes the value for the incoming beam, index $_R$ denotes the value for the reflected beam.

Reflectivity can be evaluated as

$$R_\perp = \left(\frac{E_{R\perp}}{E_{I\perp}}\right)^\star \left(\frac{E_{R\perp}}{E_{I\perp}}\right) \tag{4.3}$$

$$R_\parallel = \left(\frac{E_{R\parallel}}{E_{I\parallel}}\right)^\star \left(\frac{E_{R\parallel}}{E_{I\parallel}}\right). \tag{4.4}$$

Symbol $\star$ denotes complex conjugation. Note that these equations stand for an ideally flat surface. Because wavelength of the X-rays is comparable to atomic distances, no surface can be considered as ideally flat in the case of X-ray reflection and corrections have to be applied [29].

For the construction of X-ray optics, it is important that all materials have real part of refraction index smaller than one for X-ray radiation. It means that the phase velocity of X-ray wave is greater than the phase velocity of electromagnetic wave in vacuum c. Note that it does not mean violation of the general relativity, because this fact cannot be used for transmission of information, since the group velocity

$$v_g = \frac{\mathrm{d}f}{\mathrm{d}\lambda} \tag{4.5}$$

is never greater than c. Here, f denotes the frequency of a wave and λ denotes its length.

In general, if for the environments on Fig. 4.1 it holds $\Re(n_1) > \Re(n_2)$, the total reflection can arise and this fact is employed for construction of reflective X-ray optics. In these systems, total reflection of X-ray beams arises on the interface between air or vacuum and the surface from dedicated material.

The calculation of the refraction indices represents complex problem. Here, the mathematical model of the atomic clouds is necessary. Nevertheless, for this problem, specialised software is accessible. For example, free-of-use on-line calculator [39] can be used for this purpose.

4.2 Imaging by lobster eye

Typically, the image of the X-ray point source in the focussed arrangement obtained by LE consists of the focal cross with the bright center and the background mosaic. As an example, the reader can see the images Fig. 8.2(a), Fig. 8.28, Fig. 8.7 (image in the visible light, but similar).

The reason for this image will be clarified for the Schmidt lobster eye designed for imaging from infinity and parallel incoming X-rays, see Fig. 8.28. This situation is equivalent to the situation, where the point X-ray source lays in the focussed position of the Schmidt lobster eye designed for imaging from the finite distance, see Fig. 8.2(a).

As it has been explained, the lobster eye consists of two orthogonal sets of mirrors. Let the set of mirrors closer to the source is arranged horisontally and the second set (closer to the detector) vertically. As seen on Fig. 3.2, in each of the set of the mirrors, a ray can be reflected or it can travel directly. Of course, the ray can be also absorbed by a mirror due to the unideal reflectivity. Rays incidenting the detector (i.e. rays which are not absorbed) can be classified to four groups:

- Rays going directly through both sets of mirrors create background mosaic.

- Rays going directly through horisontal set of mirrors which are consequently reflected on some of the vertical mirrors create vertical arm of focal cross.

- Rays reflected on some of the horisontal mirrors which are consequently going directly through vertical set create horisontal arm of focal cross.

- Rays reflected on one horisontal and one vertical mirror create focal spot.

Note that a beam can reflect more than one time, however its intensity decreases with the power of the number of reflections. Twice (in general an even number times) reflected beams can create secondary focal crosses and secondary spots around the main image. Three times (in general an odd number times) reflected beams intensify the main focal cross a little, however their intensity is low and usually they are not significant.

4.3   Lobster eye geometric parameters

Each of the both sets of the lobster eye mirrors is described by these parameters (see Fig. 4.2):

- r ... radius of convergence

- a ... average spacing of mirrors

- h ... mirror deepness

- t ... mirror thickness

- n ... number of mirrors

The point $\mathbf{F}$ (focus point) have to be identical for both mirror sets, otherwise the image cannot be focussed. Also, optical axis (dash-dot line) should be the same for both sets. The point $\mathbf{C}$ (center of convergence) is different for both mirror sets. In this point it is important to say that lobster eyes are always designed for imaging from fixed distance. If LE is designed for astronomy, then the imaged source can be considered as laying in infinity and rays incoming to LE can be considered to be parallel. In this case, a simple relation $f = \frac{r}{2}$ between r and f stands for both mirror sets. LE can be also

Figure 4.2: Lobster eye geometric parameters

designed for imaging from fixed finite distance. In that case, usually one set of mirrors is parallel (its convergence radius is infinite) and the second set is designed with respect to the source distance. This design has the image focal length approximately equal to the source focal length. Also, it is possible to design LE for any source and any image focal lengths by suitable combination of radii of both mirror sets.

For optics for the visible light, the denotation focus always represents the point, where the rays incoming from infinity are concentrated. Here, we use the term focus in another meaning and it can be thought to be incorrect. For lobster eye for imaging from finite distance, as focus we denote points from where and to where the optics is able to concentrate the rays. This denotation is commonly used for lobster eye systems and it cannot cause confusion, because if the lobster eye system is designed for imaging from finite distance, it has not focus in the meaning of "point where rays incoming from infinity are concentrated". If the lobster eye is designed for imaging from infinity, than the denotation focus has the same meaning, as for optics for visible light.

It is usefull to define the following parameters[1, 10, 26]:

- Denote the angle between two adjacent mirrors with respect to the point **C** as $\epsilon = \frac{a+t}{r}$.

- Effective angle $\beta_E \approx \frac{a}{h}$ of a channel is a maximal grazing angle of directly passing beam, see Fig. 4.3(a).

- Limiting angle $\beta_L \approx \frac{2a}{h} = 2\beta_E$ of a channel is a maximal grazing angle of beam passing by one reflection, see Fig. 4.3(b).

27

It is supposed, that adjacent mirrors are approximately parallel.

(a) Effective angle   (b) Limiting angle
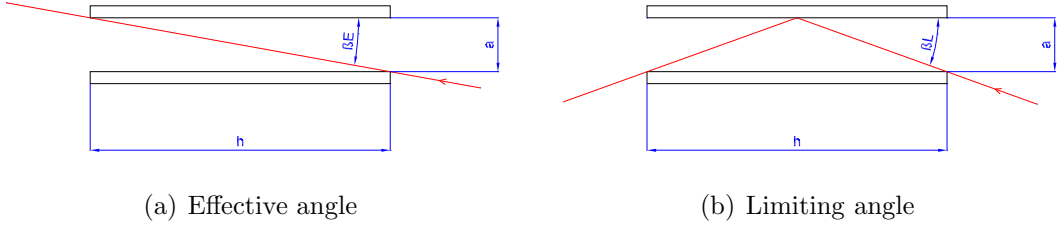
Figure 4.3: Effective and limiting angle. Mirrors are supposed to be approximately parallel

In the paper[26], it is shown that for the ideal lobster eye made from 100% reflecting blades, the size of the focal spot is equal to 2ϵ and the spot has approximately triangular shape. Hence, the angular FWHM size of the spot ω (i.e. FWHM angular resolution of the system) is equal to the ϵ and can be expressed as [10, 26]

$$\omega = \frac{a+t}{r} \tag{4.6}$$

4.4 Gain

Important quantity describing amplification of the flux in the focal spot is called gain, usually denoted as G. The gain is defined as

$$G = \frac{\text{average flux of irradiation in the focal spot}}{\text{flux of irradiation incoming to LE}}. \tag{4.7}$$

Flux means number of photons per unit time and unit area. It is necessary to define exactly which region is regarded to belong to the focal spot. In this work, the focal spot is defined as area corresponding to the projection of the central chamber of the LE [26]. In some another literature, the area of the focal spot is defined as the FWHM area [29].

For a 1-D LE system, the length of effective collecting arrea I can be approximated as $I \approx r\,\beta_L$. Size of focal spot τ can be approximately estimated as $\tau \approx a$. It leads to estimate gain as [1, 10, 26]

$$G_{1D} \approx \frac{I}{\tau} \approx 2\frac{r}{h}. \tag{4.8}$$

Because in principle, 2-D Schmidt system represents combination of two 1-D systems, its gain can be estimated as product of gains of corresponding 1-D

systems, i.e. [1, 10, 26]

$$G_{2D} \approx \frac{I_1 I_2}{\tau_1 \tau_2} \approx 4\frac{r_1 r_2}{h^2}. \tag{4.9}$$

Here, symbols r_1, r_2 denote radii of convergence of corresponding 1-D mirror subsystems. It is supposed that both subsystems have the same mirror deepness h.

4.5 Field of view

One of the two basic limits of lobster eye field of view originates in its geometry and does not depend on material of mirrors. For the definition of the corner position of FOV, see Fig. 4.4. Here, the rays are parallel to the central axis of the corner cell of LE. In this situation, direct rays can travel through the appropriate mirror set directly only at one side off the focus. For this reason, in this case one arm of focal cross vanishes and mosaic of direct beams arises only at one side of focal spot. Examples of resulting image are shown on Fig. 8.2(b), Fig. 8.27. This position is easy to found experimentally and field of view ϕ equals

$$\phi = 2\beta_C \tag{4.10}$$
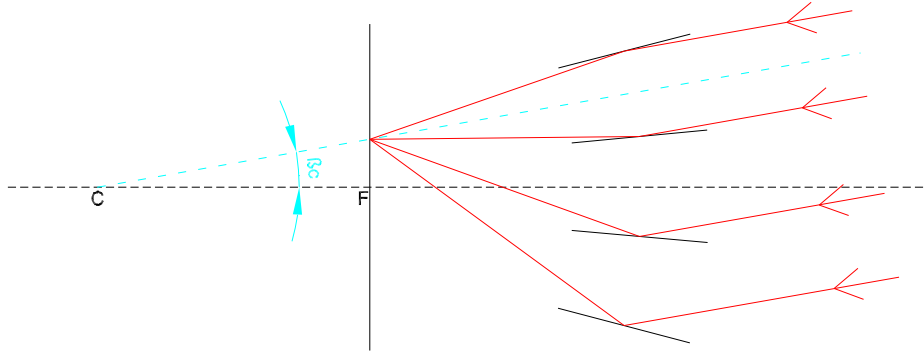
Figure 4.4: Lobster eye field of view

Using geometric parameters of LE defined in section 4.3, FOV in radians can be expressed as [S1]:

$$\phi = \frac{(a+t)(n-2)}{r} \tag{4.11}$$

29

Please note that alternative definitions of FOV exist. In particullar, we will use the following one in section 8.1. Field of view of LE (in general, of any optical system) can be defined as an angle between positions, where gain falls to a half of gain in centered position.

Chapter 5

X-ray imaging devices

Detection of X-rays is possible by many ways. Of course, for a telescope only such an X-ray detecting device can be used which allows to obtain images of the X-rays, i.e. it has to consist of many individual cells (these cells will be called "pixels") or it has to be able to get two-dimensional position information of the incomig photon in another way. Also, for the mentioned small space X-ray telescope, several key aspects of any device including the X-ray detector have to be respected:

- Size of active area

- Spatial resolution

- Overall dimensions

- Mass

- Detection efficiency

- Power consumption

For an application on a micro- or nano-satellite, the dimensions of the detector are limited to order of centimeters and the legth of the whole apparatus is limited to order of tens of centimeters.

In space telescopes, the main two types of X-ray imaging devices are being used: semiconductor pixel detectors and microchannel plates (MCP). Also, these devices seem to fit the requirements for a telescope placed on a micro- or nano-satellite. These devices will be described bellow. Rarely, another detecting devices were used, for example position-sensitive proportional counters (PSPC), scintillators, etc.

5.1 Semiconductor X-ray detectors

Semiconductor X-ray detectors are based on the effect that radiation can generate electron-hole pair in a semiconductor. As a semiconductor, silicon or germanium doped with lithium can be used. These detector are denoted Si(Li), resp. Ge(Li). Another well proven material for this purpose is cadmium telluride (CdTe) and its alloy with zinc, cadmium zinc telluride.

In principle, the detector with electrodes behaves as a semiconductor diode. In an operation, it is connected in the reverse direction. When incoming radiation generates the electron-hole pairs, these pairs can for a short time transfer the electric current and the electric pulse is generated in the circuit.

Structure of the semiconductor detector can be small ($< 100 \mu m$). It allows to fabricate a pixel detector as a network of semiconductor detectors on a semiconductor wafer.

Specifically, from the wide family of semiconductor X-ray imaging devices, the hybrid device called Medipix2 and the derived type Timepix have been selected for experiments. These devices and the related equipment were kindly provided by Institute of Experimental and Applied Physics of Czech Technical University in Prague. Thanks namely to Ing. Stanislav Pospíšil, DrSc. and Ing. Jan Jakůbek, PhD. Medipix2 and Timepix devices will be described in the following subsection.

5.1.1 Medipix2 and Timepix

The Medipix2 [19] is a semiconductor hybrid device consisting of a silicon sensor chip bonded to a read-out chip. The sensor is equipped with a matrix of 256×256 square electrodes (pixels). Each electrode (of area 55×55 μm) is connected to its own electronics made in the read-out chip. Each pixel works as a single channel analyzer with a digital counter counting individually registered photons. Medipix2 device mounted on the chipboard is shown in the Fig. 5.1. Note that the first version of Medipix had matrix only of 64x64 pixels. Also, there exists a device called Medipix2 quad. It has a matrix of 512×512 square pixels and its other properties are the same as for the Medipix2.

Medipix2 electronics

The block schematics of the electronics of the Medipix2 pixel cell is shown in the Fig. 5.2 [19]. Preamplifier performs amplification and shaping of the electric pulse generated by incoming photon in the detector. Two discrim-
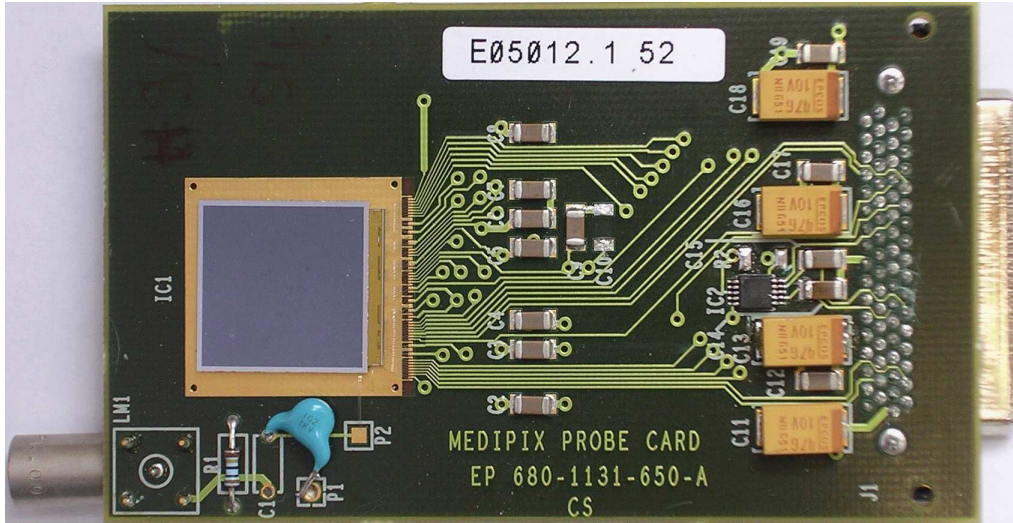
Figure 5.1: Medipix2 device mounted on the chipboard

inators with appropriate logic circiuts allow to set an energy window. One dicriminator defines the top energy level and the second one defines the bottom energy level. The 14-bit shift register with related logics works as a digital counter. Each individual gamma particle belonging to the selected energy window is counted. This concept allows to use long acquistion times, which are limited only by the counter range. Maximal count is 8001 for the Medipix 2.0 detector and 11810 for the Medipix2.0 MXR detector.

Medipix2 spectral properties

Medipix2 is not convenient for acquiring the spectra (the timepix is more convenient). With the Medipix2, the spectra can be acquired only by the threshold scan, i.e. by the series of measurements with the threshold set to various values. This method requires a stable source. Threshold scan takes a long time and gives the integral spectra. To get the differential spectra, the integral spectra must be numerically differentiated, which increases the noise. An example of the integral spectra acquired by the Medipix2 device is shown in the Fig. 5.3. There are shown fluorescent spectra of the cadmium and the indium illuminated by an X-ray source. The measurement has been performed at the Institute of Experimental and Applied Physics of CTU in Prague. The spectra from the Fig. 5.3 differentiated are shown on the Fig. 5.4. It is seen that the sharp energy is smeared to gaussian peak with FWHM approx. 3-5 keV. This effect is caused by the basic properties
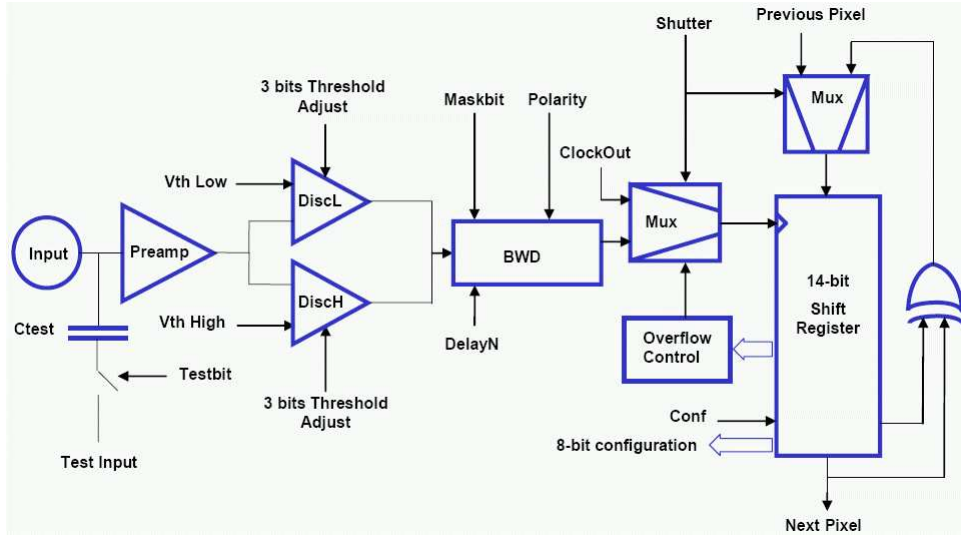
Figure 5.2: Medipix2 pixel cell electronics [19]

of the silicon detector at room temperature and it limits the spectroscopic resolution.

The left side "tail" is also seen on the Fig. 5.4 . This tail appears for the following reason: if the edge between two or more pixels is hit, the generated charge is shared among all adjacent pixels. This effect is called "charge sharing effect" (see [25]) and is is hard to neglect.

Heat oscillations generate electron-hole pairs in the silicon sensor chip and these pairs transfer electric current. This effect appears as noise at the lowest energies. For this reason, the minimal detectable energy is approx. 3.5 keV. Under this level, the noise exceeds the useful signal. Conventional Si detectors can be cooled to decrease heat oscillations to allow detection at lower energies. However, Medipix electronics is not designed for working at low temperatures. Another problem is that aging caused mainly by radiation damage increases the minimal detectable energy. For use in space, it is necessary to take into account this fact and not use the device at the minimal energy 3.5keV but a little higher, for example 4.5keV.

The maximal detectable energy is not given exactly. The problem is the detection efficiency decreaes at higher energies because of decreasing of the apsorbtion efficiency of the sensor. The absorption efficiency as a function of the photon energy for miscellaneus materials and thickness is shown on the Fig. 5.5 [23].
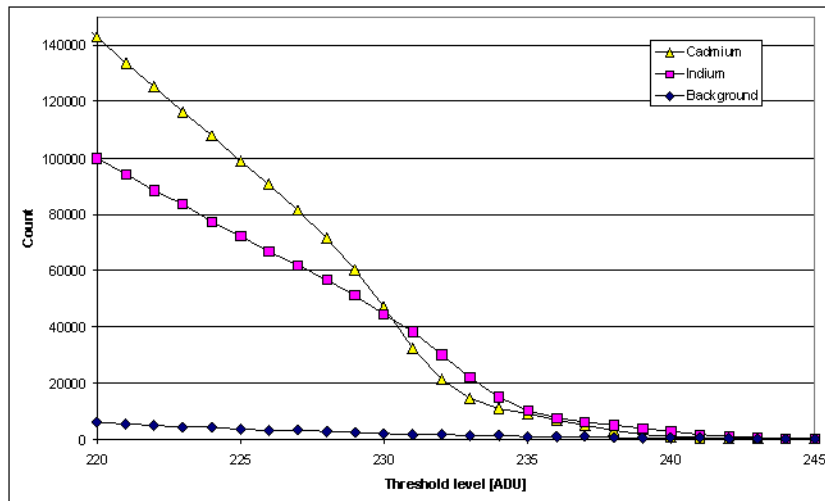
34

Figure 5.3: Integral X-ray fluorescent spectra of Cd and In acquired by Medipix2 [S5]

Timepix

The Timepix device [20] is derived from the Medipix2. Both devices use the same sensor chip and for this reason they have the same basic properties (matrix size, energy range, energy resolution, etc.).

The electronics in the Timepix is modified (see Fig. 5.6) [20]. In the Timpeix, the high threshold discriminator is not included. Contrary to the Medipix2, the logic part of Timepix electronics provides three modes: event counting (single counting mode as Medipix), arrival time mode and time over threshold (TOT) mode.

In TOT mode, duration of pulse from preamplifier is measured and incoming particle energy can be determined. Differential spectra are acquired. If the charge generated by an incoming particle is shared among more pixels, energy detected in all pixels in the generated cluster can be summed [11]. Such a way, charge sharing effect is neglected. However, in the TOT mode, the readout speed must be sufficient so that events from more than one particles have not been detected by one pixel. An example of the acquired spectra is shown in the Fig. 5.7. Here, spectrum of the [241]Am source measured by the Timepix in TOT mode is shown. The measurement has been performed at Institute of Experimental and Applied Physics of CTU in Prague.
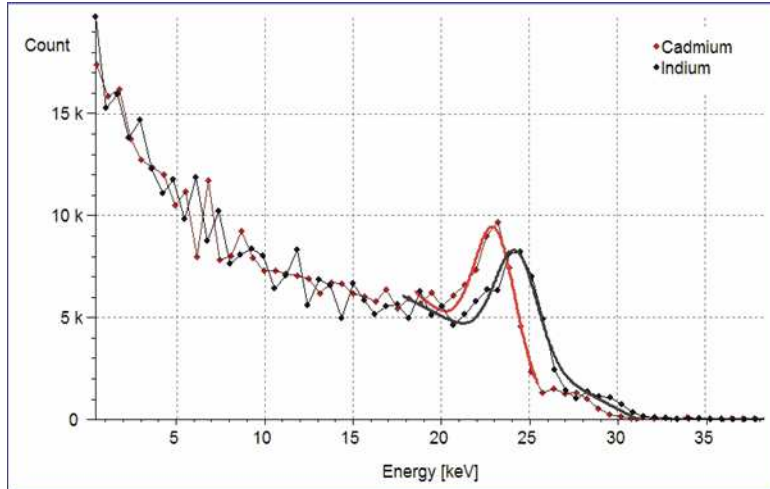
Figure 5.4: Differential spectra calculated from the integral spectra measured by Medipix2 [S5]

5.2 Microchannel plate

The microchannel plate (MCP) [35] was originally developed as an amplification element for image intensification devices. Moreover, MCP have direct sensitivity to energetic photons (including X-ray) and charged particles.

The base component of the MCP is a plate from material of high electric resistance containing a net of holes (channels) leading from one side of a plate to the oposite side Fig. 5.8 [35]. Channel axes are typically normal to, or biased at a small angle ($\sim 8°$) to the MCP input surface. Usually, the plate is fabricated from a lead glass. Typical thickness of this plate is a few millimeters and typical diameter of channels is around 10 microns. Front and rear surfaces of the MCP are coated by metal and operate as electrodes. Electrodes powered by electric voltage creates electric field in each channel. The total electric resistance between these electrodes is in the order of $10^9\Omega$.

Each channel operates as an electron multiplier, its principle is drawn on Fig. 5.9 [35]. When radiation hits the surface of the channel, electrons are emitted. Emitted electrons are accelerated by the electric field and their next hits of the channel surfaces produce subsequent electron emissions. These electrons can be converted to a visible light using a scintillator. Then the visible image is acquired by a common visible light pixel detector (CCD, CMOS). Also, MCP can contain a network of anodes for a direct detection of the incident photon position.
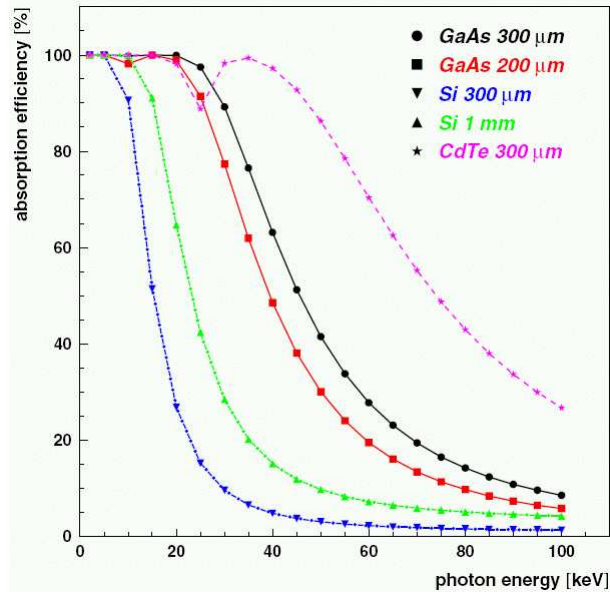
Figure 5.5: Absorption efficiency as the function of the photon energy ranking from 5 keV to 100 keV [23]. Typically, Medipix2 and Timepix use 300 mm thick Si.

MCP detectors allow ultra-high time resolution (<100ps) and good spatial resolution (up to order of tenth of microns), however their detection efficiency for soft X-rays is low (typically 5-15%)[35].

The detection efficiency can be increased by using two microchannel plates consecutively. This type of construction is called Chevron MCP [5]. Some MCP devices exist that use even three microchannel plates.

Figure 5.6: Timepix pixel cell electronics [20]

Figure 5.7: Differential spectrum of Am241 acquired by Timepix device in TOT mode
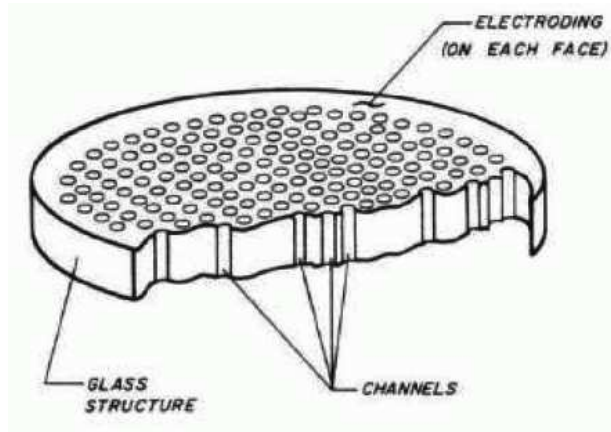
Figure 5.8: Microchannel plate [35]
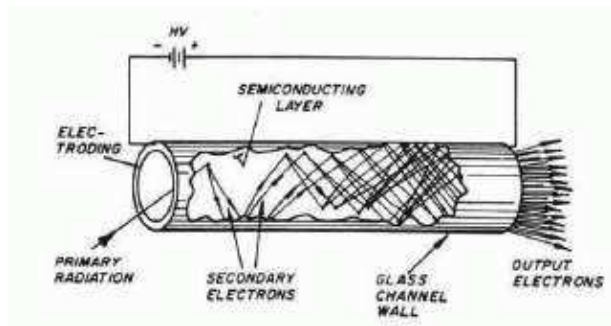
Figure 5.9: Principle of electron multiplier [35]

Chapter 6

Telescope module prototypes

6.1   Lobster eyes

For our experiments, Rigaku Innovative Technologies Europe, s.r.o. provided
three prototypes of lobster eyes listed in Tab. 6.1. We kindly thank this com-
pany, namely to doc. Ing. Ladislav Pína, DrSc., Ing. Adolf Inneman, PhD.
and Ing. Veronika Semencová.

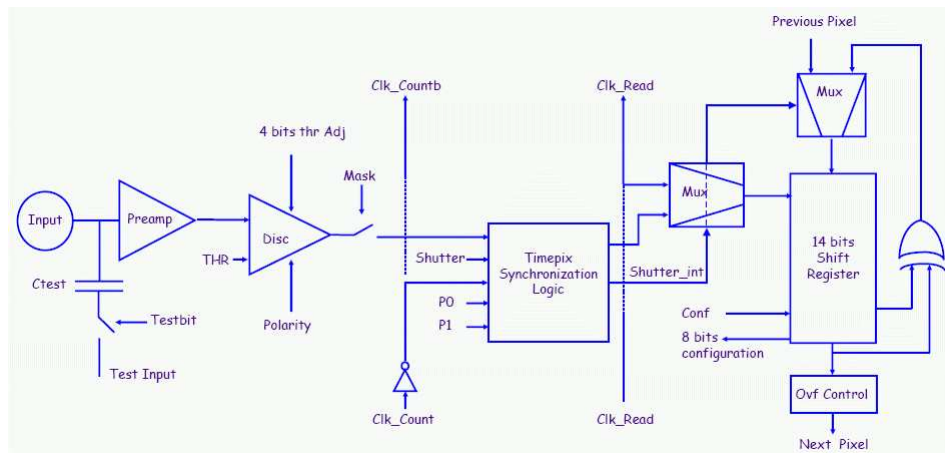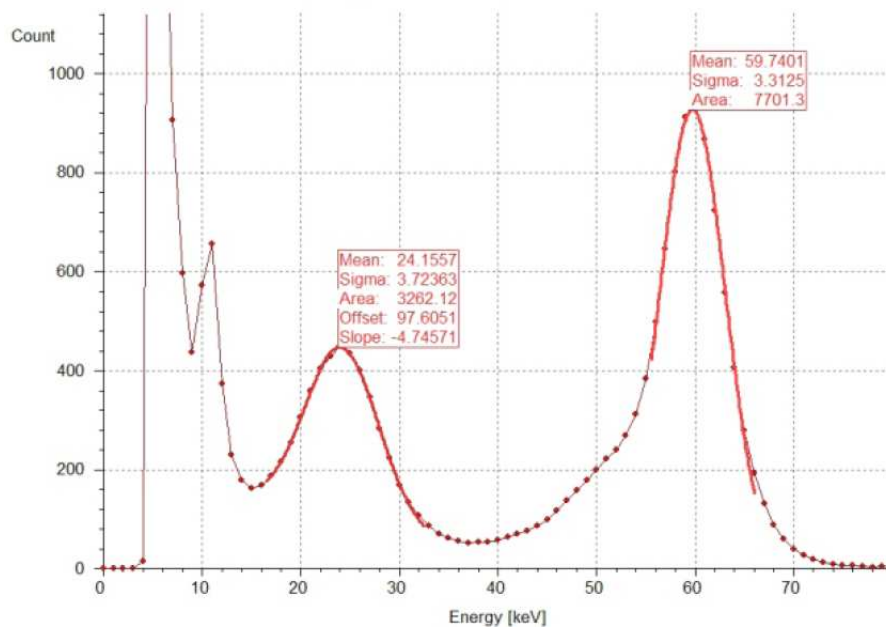   All these LEs use gold coated glass as the mirroring plates.

denotation	optimal energy [keV]	object focus [mm]	image focus [mm]	number of plates in each set	plates dimensions [mm×mm]	plates spacing [μm]	plates thickness [μm]
P-25	1	∞	250	60	24×24	300	100
P-90	8	∞	900	60	24×24	300	100
L.U.N.D.	8	400 -600	400 -600	60	22×30	300	100

Table 6.1: Lobster eyes available for experiments

   Experiments with the lobster eye L.U.N.D. were performed on the optical
bench. For the lobster eyes called P-25 and P-90 were two experimental
modules called XTM-25 and XTM-90 manufactured in Rigaku Innovative
Technologies Europe, s.r.o. We kindly thank this company, namely to Ing.
Jiří Maršík.

6.2   Experimental module XTM-90

The experimental module XTM-90 manufactured by the Rigaku Innovative
Technologies Europe, s.r.o. consists of the aluminium body tube, the lobster

eye P-90 (see Tab. 6.1) with the mounting device and the detector Medipix2 with the mounting device. Also, the adaptor for a photographic camera for the tests in the visible light was manufactured in Rigaku Innovative Technologies Europe, s.r.o. The detecting device Medipix2 was kindly provided by the Institute of Experimental and Applied Physics of the Czech Technical University in Prague. Thanks namely to Ing. Stanislav Pospíšil, DrSc. and Ing. Jan Jakůbek, PhD.

Figure 6.1: Module XTM-90 on optical bench

6.3 Experimental module XTM-25

The experimental module XTM-25 manufactured by the Rigaku Innovative Technologies Europe, s.r.o. consists of the aluminium body tube, the lobster eye P-25 (see Tab. 6.1) with its mounting device and the adaptor for a photographic camera for tests in the visible light.

Figure 6.2: Module XTM-25 on optical bench

Chapter 7

Simulation program

To assess the experiments, author of the dissertation developed the simulation program. The program simulates operation of Schmidt type LE [26] in a parallel X-ray beam. The program is presented in this chapter, experimental results follow in chapter 8. The program is also being used by Rigaku Innovative Technologies Europe, s.r.o..

7.1 Used principles

In general, for simulation of X-ray focussing systems, ray-tracing methods can be used [45] as for focussing systems for visible light. A Schmidt's lobster eye has an important property, it consists of two orthogonal subsystems. This fact allows to simplify the problem. Because each of the two subsystems is in principle one-dimensional, its operation can be expressed by one-dimensional matrix. Operation of the whole LE can be expressed as outer product of these two one-dimensional matrices. Program has been developed in the freeware C++ compiler and development environment Dev-C++ [36]. For all real values, the variable of type "double" (IEE754-1985 64-bit real variable [44]) were used.

In this chapter, the longitudal axis (i.e. optical axis if the whole simulated setup is centered) is denoted z. Lateral axis of the one-dimensional system is denoted b. Here, denotation x or y is not used to prevent confusion during transformation from the two one-dimensional systems to the one two-dimensional system.

7.2 Simulation of one-dimensional lobster eye system

In the simulation program, each mirror is represented by the data structure containing 2-D coordinates of its vertices. The mirror set is represented as an array of these structures.

Detector is represented as an 1-dimensional field of real values, each item of the field represents detected intensity in the corresponding pixel. Detector surface is supposed to be perpendicular to z-axis. The detector z-position can be set arbitrarily. The pixel size is also stored.

As mentioned in section 4.2, part of image is due to direct beams, part by one-time reflected beams. Multiplically reflected beams are not token into accout. Incoming radiation is assumed to be unitary, it means that the direct perpendicular hit of detector pixel causes detection of intensity 1.

7.2.1 Direct beams

After initialising the mirror and detector parameters, effect of direct beams is simulated.

Simulated situation is shown on Fig. 7.1. Here, α denotes slope of a mirror
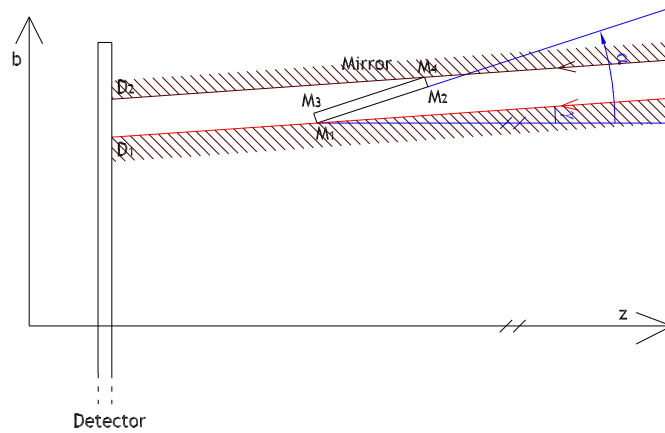

Figure 7.1: Principle of simulation of direct beams

relative to z-axis, γ denotes slope of rays relative to z-axis. Both these angles are oriented, positive value means anti-clockwise orientation.

We have found it is very useful to invert the problem. First, the field representing detector is filled by $\cos(\alpha)$ to simulate the whole detector be

illuminated by radiation of unit flux impacting at angle α. Next, the effect of shielding by mirrors is calculated. This calculations are performed as follows.

First, b-positions of the points $\mathbf{D_1}$ and $\mathbf{D_2}$ are evaluated. If $\alpha \geq 0$, then b-positions of points $\mathbf{D_1}$ and $\mathbf{D_2}$ can be expressed as

$$
\begin{align}
D_1 &= M_{1b} - (M_{1z} - D_z)\tan(\gamma) \tag{7.1}\\
D_2 &= M_{4b} - (M_{4z} - D_z)\tan(\gamma) \tag{7.2}\\
&\tag{7.3}
\end{align}
$$

If $\alpha < 0$, then the points $\mathbf{M_2}$ and $\mathbf{M_3}$ have to be used instead of $\mathbf{M_4}$ and $\mathbf{M_1}$. Symbol D_z denotes z-position of the detector. Symbol D_b denotes b-position of the first pixel of the detector.

When the positions are evaluated, they are re-calculated to position on detector in pixels using equations

$$
\begin{align}
p_1 &= \operatorname{int}\left(\frac{D_1 - D_b}{s}\right) \tag{7.4}\\
q_1 &= D_1 - D_b - \frac{p_1}{s} \tag{7.5}\\
p_2 &= \operatorname{int}\left(\frac{D_2 - D_b}{s}\right) \tag{7.6}\\
q_2 &= D_2 - D_b - \frac{p_2}{s} \tag{7.7}
\end{align}
$$

Here, s denotes the size of a pixel. Function $\operatorname{int}(x)$ denotes the largest integer number less or equal to x. Variables p_1 and p_2 denote index of pixel corresponding to points $\mathbf{D_1}$ and $\mathbf{D_2}$. Values q_1 and q_2 are always within the interval $[0, 1)$ and they denote relative positions of the points $\mathbf{D_1}$ and $\mathbf{D_2}$ within pixels.

Now the following set of conditions is tested:

- If $p_1 \neq p_2$ then $1 - q_2$ is subtracted from intensity in the pixel of index p_1, and q_2 is subtracted from intensity in pixel of index p_2. If, moreover, $p_1 < p_2 - 1$ then all pixels of indices between $[p_1 + 1, p_2 - 1]$ are zeroed.

- If $p_1 = p_2$ and $q_1 < q_2$ then value $q_2 - q_1$ is subtracted from intensity in pixel of index $p_1 = p_2$.

- If $p_1 = p_2$ and $q_1 = q_2$, nothing is performed (very unprobable situation).

After this process, it is tested whether intensity in each pixel is non-negative. If not, related pixels are zeroed.

7.2.2 Reflected beams

As the mirrors are considered to be plain (i.e. they are supposed not to be curved; note however that their non-zero thickness will be taken into account), the sufficient task is to calculate positions of reflections of individual mirrors. The situation is described on Fig. 7.2. Here, α denotes the slope of
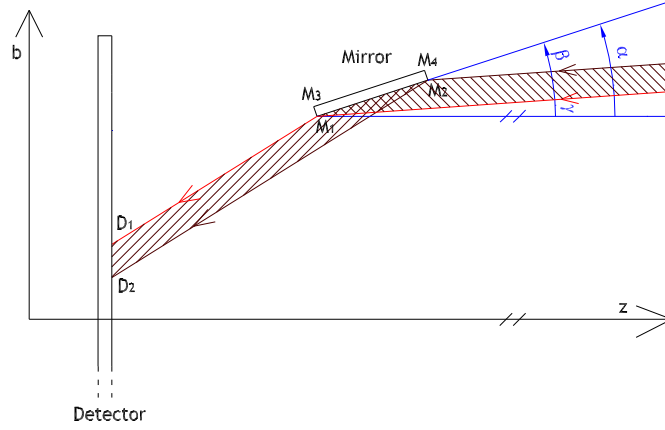

Figure 7.2: Principle of simulation of reflected beams

the mirror relative to z-axis, β denotes the grazing angle and γ denotes the slope of the rays relative to the z-axis. All named angles are oriented, positive value means anti-clockwise orientation. Symbols $\mathbf{M_1}$, $\mathbf{M_2}$, $\mathbf{M_3}$, $\mathbf{M_4}$ denote vertices of mirror. Points $\mathbf{D_1}$ and $\mathbf{D_2}$ are the border points of the reflection.

Using simple trigonometric calculations, position of the points $\mathbf{I_1}$ and $\mathbf{I_2}$ can be expressed as

$$
\begin{align}
D_{1b} &= M_{1b} - (M_{1z} - I_{1z})\tan(2\beta + \gamma), \tag{7.8} \\
D_{2b} &= M_{2b} - (M_{2z} - I_{2z})\tan(2\beta + \gamma), \tag{7.9} \\
\beta &= \alpha - \gamma, \tag{7.10} \\
\alpha &= \arctan\left(\frac{M_{2b} - M_{1b}}{M_{2z} - M_{1z}}\right). \tag{7.11}
\end{align}
$$

As the mirror is supposed to have a finite thickness, it is necessary to test, which side of the mirror reflects. If $\beta < 0$ then beams hit the oposite side of a mirror and symbols $\mathbf{M_1}$, resp. $\mathbf{M_2}$ in eqs. 7.8-7.9 have to be identified with the appropriate points on the illuminated side of mirror.

In the calculation of the reflections, one important correction have to be made, since reflection can be shaded by an adjacent mirror. The situation
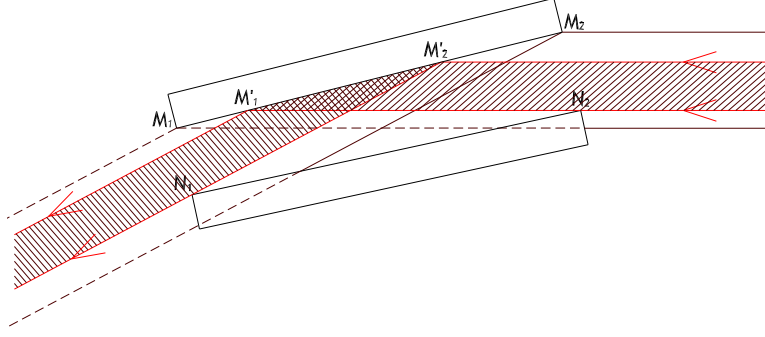
45

Figure 7.3: Effect of shading by adjacent mirror

is shown on Fig. 7.3. On the Fig. 7.3, it is shown that the whole surface between points $\mathbf{M_1}$ and $\mathbf{M_2}$ does not act in the reflection. Only the effective arrea bordered by the points $\mathbf{M'_1}$ and $\mathbf{M'_2}$ have to be taken into account.

In the detail, this procedure will be specified for the beams parallel to the z-axis. Positions of the points $\mathbf{M'_1}$ and $\mathbf{M'_2}$ are calcualated using the equations

$$t = \frac{M_{2b} - M_{1b}}{M_{2z} - M_{1z}}, \tag{7.12}$$

$$q_1 = M_{1b} - t\, M_{1z}, \tag{7.13}$$

$$q_2 = N_{1b} - 2t\, N_{1z}, \tag{7.14}$$

$$M'_{1z} = \frac{N_{2b} - q_1}{t}, \tag{7.15}$$

$$M'_{1b} = M_{2b}, \tag{7.16}$$

$$M'_{2z} = \frac{q_1 - q_2}{t}, \tag{7.17}$$

$$M'_{2b} = t\, M'_{2z} + q_1. \tag{7.18}$$

If $M'_{1z} > M_{2z}$ or $M'_{2z} < M_{1z}$ or $M'_{1z} > M'_{2z}$ then the arrea bordered by points $\mathbf{M_1}$ and $\mathbf{M_2}$ is shaded completely and the corresponding foil does not contribute to reflection at all.

If $M'_{1z} < M_{1z}$ then the theoretical position of the point $\mathbf{M'_1}$ lays outside the mirror and the point $\mathbf{M_1}$ is not shaded, this correction for the point $\mathbf{M_1}$ is not used and the position of the point M_1 itself has to be used for calculations.

Similarly, if $M'_{2z} > M_{2z}$ then the theoretical position of the point $\mathbf{M'_2}$ lays outside the mirror and the point $\mathbf{M_2}$ is not shaded and the position of the point $\mathbf{M_2}$ itself is used for calculations.

46

7.3 Calculation of reflecting coefficient

The simulation program allows to use one of the three methods of calculation of the reflecting coefficient. At first, all mirrors can be simulated to be ideal mirrors of 100% reflectivity. This was used to test the program by comparing its results to the results of the equations mentioned in chapter 4. The second way is similar, it allows to set any constant reflecting coefficient.

The third method is intended for simulation of behavior at the energy of 930eV. It is one of the lines used in the tests in XACT (see section 8.3) and it is the value near to the optimal energy for the lobster eye P-25. In this case, the linear approximation of the curve of the reflectivity for gold at the energy of 930eV obtained from [39] is used. The error of the approximation is less than 1%. This method is applicable only when all mirrors are illuminated at small grazing angle, less than approx. 3°. Note that the lobster P-25 illuminated in the center position fulfills this condition.

The fourth method allows to simulate any material. In this case, program allows to import reflectivity data from the source [39]. Between the given points, the linear interpolation is performed.

7.4 Functionality test

Functionality of the simulation program has been tested for the lobster eye P-25 (see Tab. 6.1). For this lobster eye, equation (4.9) gives the gain as 1732. Equation (4.9) is derived from such model of the lobster eye, which consist of infinite number of infinitely thin, ideally reflecting mirrors and their spacing is infinitely low [26]. At next, shading of the mirrors by the adjacent mirrors is neglected here. Due to these approximations, in the paper [26] is expected the real gain will be less than the value given by this model.

The simulation program allows to consider the mirrors to be infinitely thin and ideally reflecting. Also, simulation of the shading among the mirrors can be switched off. If it is done and the mirrors deepness h, their average spacing a, number of them and their radii of convergence r_1, r_2 are set to the values of the lobster eye P-25, the program computes gain as 1479. This result is in rough corelation with the result of equation (4.9). The result of the simulation is less as it has been expected.

If thickness of the mirrors is taken into account, their non-ideal reflectivity is simulated and the shading is simulated, the gain reaches 764 for the photons of energy 930eV. Further results for this lobster eye are presented in section (8.3). Here, comparison to the values obtained experimentally is given too.

Chapter 8

Lobster eye experimental tests

8.1 Imaging from finite distance

The first tests were performed with the lobster eye L.U.N.D. (see Tab. 6.1) designed for imaging from finite distance. This lobster eye was kindly provided by Rigaku Innovative Technologies Europe, s.r.o. and Measurements were performed in their laboratories. We kindly thank this company, namely to doc. Ing. Ladislav Pína, DrSc., Ing. Adolf Inneman, PhD. and Ing. Veronika Semencová. For these experiments, X-ray detecting device Medipix2 was kindly provided by the Institute of Experimental and Applied Physics of the Czech Technical University in Prague. We kindly thank this institution, namely to Ing. Stanislav Pospíšil, DrSc. and Ing. Jan Jakůbek, PhD.

Used lobster eye L.U.N.D. (see Tab. 6.1) has the similar design as the lobster eye P-90 (see Tab. 6.1) intended for imaging from infinity.

Goals of these measurements were to test the basic functionality of the lobster eye with Medipix2 at the energy of 8keV, and to obtain the basic imaging characteristic. Note that measurement of the image distortion of the LE as the function of the source position represents an original type of experiment. Any similar experiment with LE has not been published previously.

8.1.1 Experimental setup

The used setup consists of the X-ray tube source with a copper target, lobster eye optics and Medipix2. X-Ray tube was set to accelerating voltage 40kV.

In all measurements, the detector and X-ray tube was fixed in the focuses of the optics (see section 4.3 for note of meaning of the term focus used here). Optics is located on the device allowing vertical and horizontal translations. Used optics L.U.N.D. (see Tab. 6.1) has outer dimensions
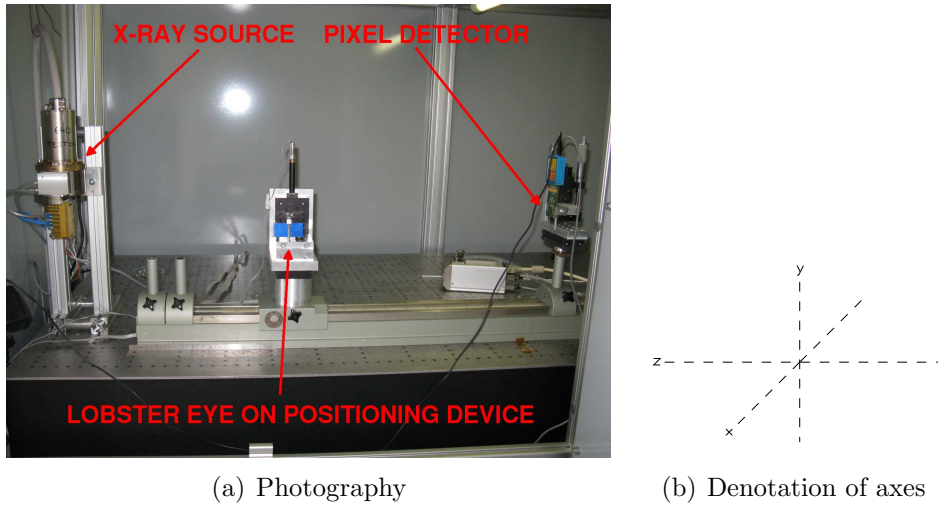
(a) Photography

(b) Denotation of axes

Figure 8.1: Setup for imaging from finite distance

65x30x30mm. Distance between the edge of the optics and the X-ray source was 455mm, distance between the edge of the optics and the detector was 580mm.

Axes are denoted as follows (see Fig. 8.1(b)): z-axis is the optical axis of the whole setup, y-axis is the vertical axis and x-axis is the lateral horisontal axis.

8.1.2 Spatial resolution and field of view

The image obtained with the centered optics and filtered by the median filter with a cell of 3×3 pixels is shown on (Fig. 8.2(a)). It is seen that the optics is operative at the chosen energy (approx. 8keV). Intensity along the horisontal axis passing through the centre of the cross is drawn on the Fig. 8.3. To suppress the noise, data were processed in superpixels of 1 pixel width (x-size) and 3 pixels height (y-size). The FWHM of the main peak is 19 pixels, it corresponds to the angle distance of 6.5″. It is a principal limit of the angular resolution.

To determine the field of view, corner positions of the optics (see chapter 4.5) were found. In each of these positions, the center of the cross lays at the one of the borders of the image (see Fig. 8.2(b)). Distance between these positions is 16.8mm. If, for the sake of simplicity, it is supposed that the optics lays at the middle of the distance between the X-ray tube and detector, i.e. at 550mm, field of view can be determined as approx. 1.7°.
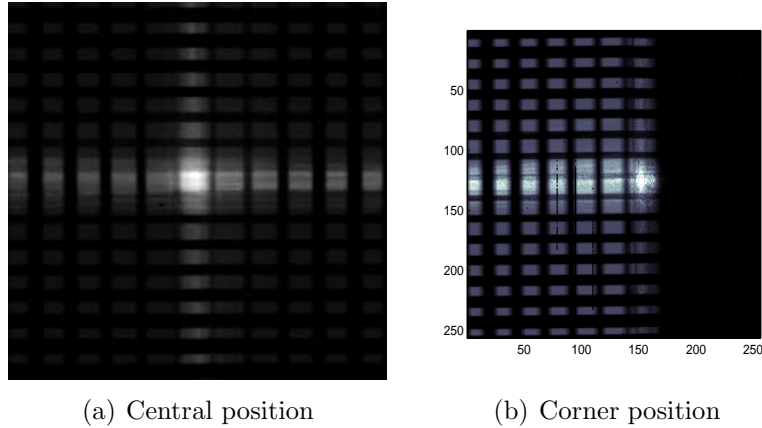
(a) Central position   (b) Corner position

Figure 8.2: Basic images obtained by lobster eye L.U.N.D.

8.1.3 Image distortion and intensity

For the applications, the image distortion and intensity as a function of the source position have to be measured, because these effects must be corrected.

The X-ray tube source and the detector were situated at fixed points. The optics was being moved to various positions in x-axis (vertical) and y-axis to simulate imaging from various source positions. This setup provides imaging with the scale of roughly $1 : 1$, for this reason the detector might not be moved because if the LE is moved to any position, the relative position between the detector and the LE is also changed by the same distance.

In each position of the LE, position of the centre of the cross on the image have been determined as follows: first, the image was filtered by the median filter with the cell of 3×3 pixels. Then, for each box of the size 5×5 pixels, the total intensity is calculated. Center of the box of the highest total intensity is assumed as the center of the focal spot.

Shifts of the centers of the crosses from the ideal positions (i.e. with linear optics) to the measured positions are shown on the (Fig. 8.4(a)).

On the (Fig. 8.4(b)), the result of simulation is shown. The point source was virtually moved across the sky and for each position the raytracing was used to get its image. Ideal position and position measured at the images were compared. Here, the code used for the simulation was XAnn3D [45] and the simulation was performed in collaboration with Mgr. Libor Švéda, PhD from Faculty of Nuclear Sciences and Physical Engineering of CTU and from the company Elya solutions, s.r.o. Author thanks him kindly for the help.

The graphs of the measured data (Fig. 8.4(a)) and the simulation (Fig. 8.4(b)) are similar. This fact indicates that the optics behavior relates to the assump-
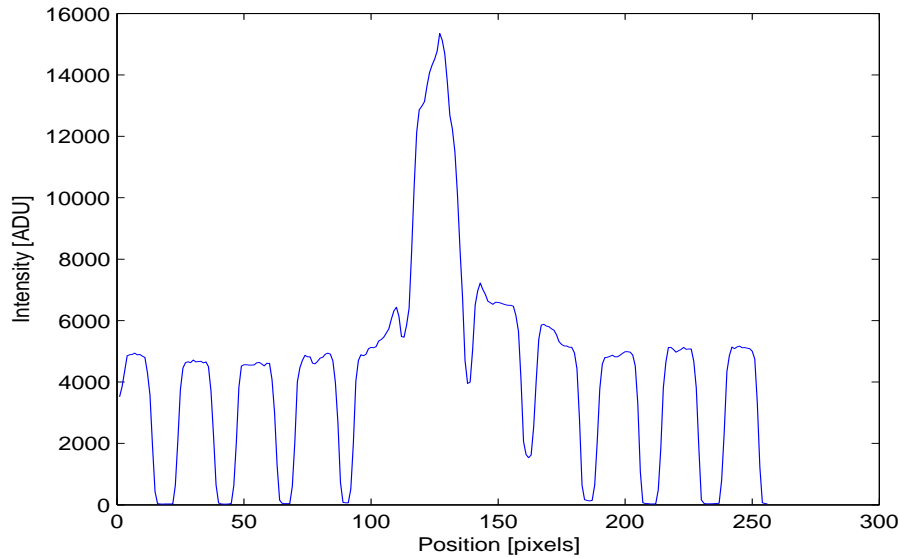
50

Figure 8.3: Graph of intensity from Fig. 8.2(a)

tions. The assymetry of the graph (Fig. 8.4(a)) indicates that the foils in the optics have some distortions.

Relative intensity of the cross centre as function of optics position is shown on Fig. 8.5. Intensity drops to a half of the intensity at the centered position roughly at corner positions of the optics determined in section 8.1.2. Hence, the field of view defined by positions where decrease of an intensity to a half occurs is about the same as deduced from corner positions of the optics.

8.1.4 Assesment

For the presented results, the lobster eye optics designed for imaging from focus to focus has been used. The similar type of optics, but designed for imaging from infinity to focus is planned for the tests for the space X-ray telescope. The optics has been used with the Medipix2 sensor device. Results of the measurements indicate, that Medipix2 is suitable for the lobster eye optics at the chosen energy 8keV. At this energy, the obtained field of view and spatial resolution have been identified. Image of distortion depending on incoming angle has been measured. Experimental results correspond to simulations. Image of distortion and intensity depending on incoming angle has been measured.
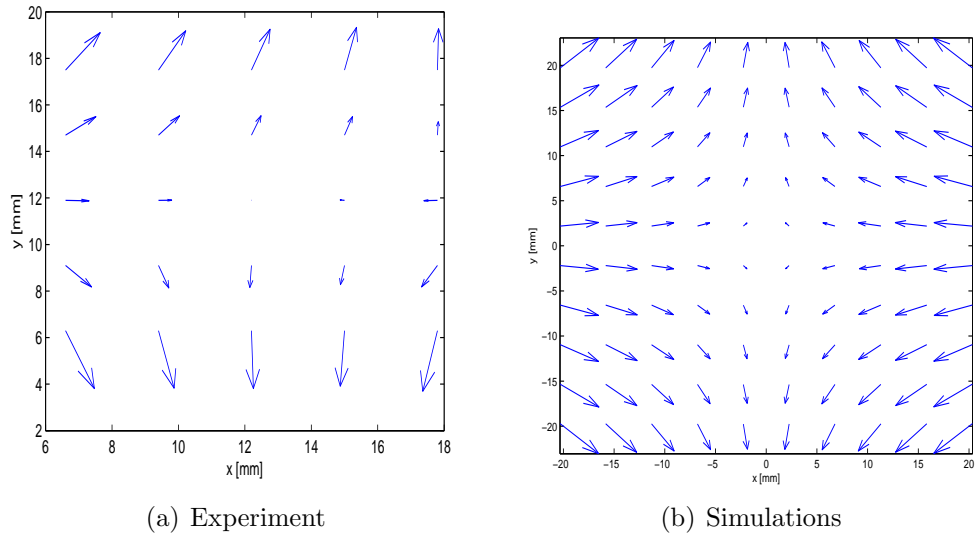
(a) Experiment

(b) Simulations

Figure 8.4: Image distortion. Arrows represents shifts of focal spot position from its ideal position
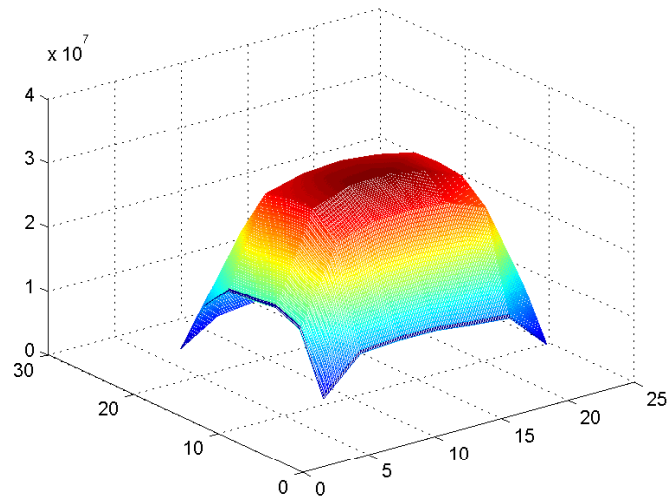

Figure 8.5: Relative intensity of the cross centre as a function of optics position

52

8.2 Tests of telescope prototypes in visible light

Modules XTM-25 and XTM-90 (see chapter 6) were tested in visible light. Note that gold coated surfaces in used lobster eyes P-25 and P-90 (see table Tab. 6.1) reflect visible light too. However, their reflectivity for the visible light is different than for the X-rays. For this reason, tests in visible light show basic functionality and they can give rough information about spatial resolution. Usually, spatial resolution of LE is better in X-ray than in visible light, since in visible light, some unwanted effects (mainly diffraction effects) appear.

8.2.1 Experimental setup

Experiments have been performed in the laboratories of Division of Precision Mechanics and Optics of Department of Instrumentation and Control Engineering of Faculty of Mechanical Engineering of the Czech Technical University in Prague.

In place of the X-ray pixel detector, the camera Cannon350D EOS was used. This camera contains CCD chip of diameter 15x22.5mm with the resolution of 2304×3456 pixels. Its pixel size is approx. 6.51μm. The whole setup consists of the light source, the aperture, the collimator and the tested module. The setup was placed on the optical bench as it is photographed on Fig. 8.6

As the apertures, a metal (opaque) plate with single hole of diameter 0.5mm and three metal plates with two holes of the same diameter and variant distances have been used. The collimator had focal length 150cm. In this configuration, the light source with the single hole aperture can be regarded as a point source placed at infinite distance. Light source with aperture with two wholes can be regarded as two point sources at infinity. Distances of the holes have been chosen to represent sources of angle distances $10'$, $20'$ and $30'$.

8.2.2 Results

Module XTM-25

The basic image obtained with single hole aperture and filtered by the median filter with the cell of size 5×5 pixels is shown on Fig. 8.7.

Intensity along the horisontal axis passing through the centre of the cross is drawn in the Fig. 8.8. FWHM size of the peak in this graph corresponds to
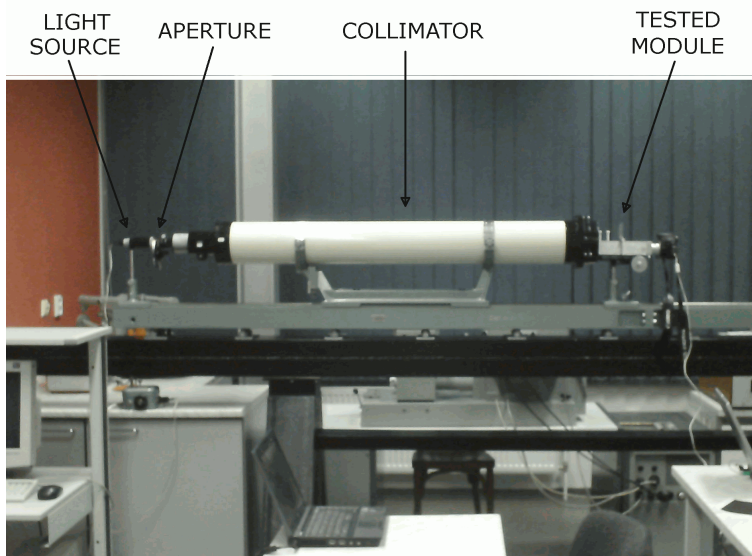
Figure 8.6: Overall experimental setup

the distance of 1.21mm and it corresponds to the angle of view of 17'. This value represents the FWHM angular resolution.

To simulate graph of intensity of two point sources, these data are drawn shifted and also sum of both data sets is drawn. The depicted situation corresponds to the situation, when the angle between the sources is approx. 16'. It has been indentified as the limit position where the sources can be resolved, if the intensity is demanded to fall between peaks to 80 % of the peak level.

The resolution was tested experimentally with two-hole apertures with various hole distances. Resulting image for holes of angle distance 30' is shown on Fig. 8.9. Graph of intensity along the horisontal axis is shown on Fig. 8.10. The minimal value of the intensity between the main peaks is approx. 62% of intensity of the lower peak. Sources are therefore well resolved.

The analogous results for the angle distance 20' are shown on Fig. 8.11 and Fig. 8.12. The minimal value of intensity between the main peaks is approx. 74% of intensity of the lower peak. Sources are well resolved, however they are near the limit of resolvability.

Analogous results for angle distance 10' are shown on Fig. 8.13 and Fig. 8.14. The minimal value of intensity between the main peaks is approx. 94% of intensity of the lower peak. Sources are not resolved.
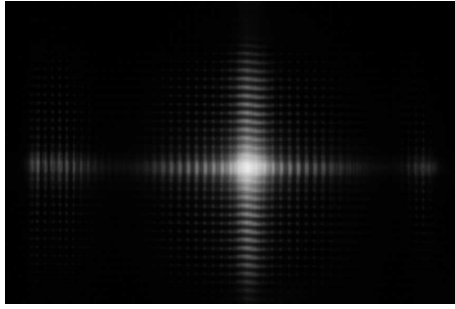
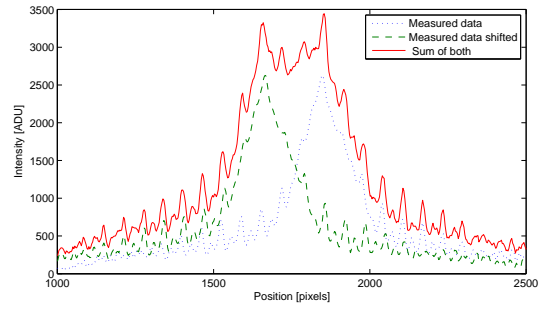Figure 8.7: Image from XTM-25 with single aperture

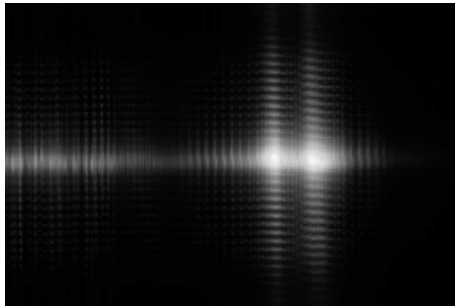Figure 8.8: Estimation of spatial resolution of XTM-25 in horizontal axis

Figure 8.9: Image from XTM-25 with two-hole aperture with angle distance 30'
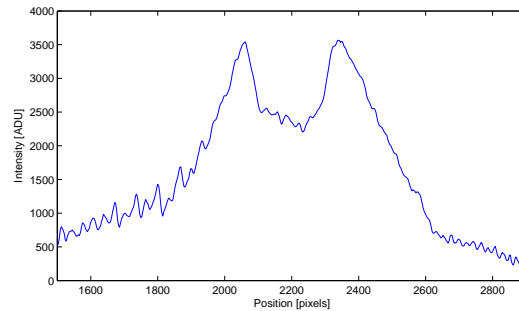

Figure 8.10: Graph of intensity from Fig. 8.9

Module XTM-90

The basic image obtained with the single-hole aperture and filtered by the median filter with the cell of size 5×5 pixels is shown on Fig. 8.15. The mean FWHM of the main spot corresponds to angle of view approx. 17'.

Intensity along the horisontal axis passing through the centre of the cross is drawn on the Fig. 8.16. FWHM size of the peak in this graph corresponds to the distance of 4.36mm and it corresponds to the angle of view of 17'. This value represents the FWHM angular resolution.

To simulate distribution of intensity for two point sources, these data are drawn shifted and also sum of both data sets is drawn, as it has been done for the module XTM-25. Drawn situation corresponds to the situation, when the angle between the sources is approx. 19'. It has been found that it is the limit position, where the sources can be resolved, if it is demanded the intensity to fall between peaks to the 80% of level of the peak.
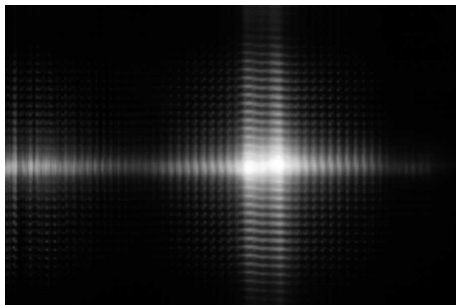
Figure 8.11: Image from XTM-25 with two-hole aperture with angle distance 20'
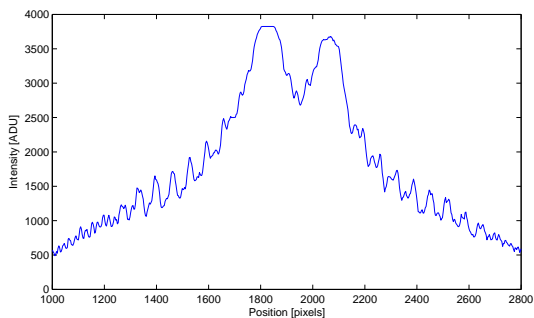

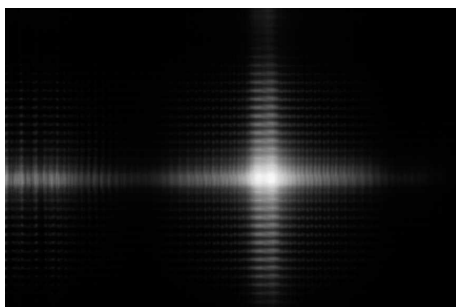Figure 8.12: Graph of intensity from Fig. 8.11

Figure 8.13: Image from XTM-25 with two-hole aperture with angle distance 10'
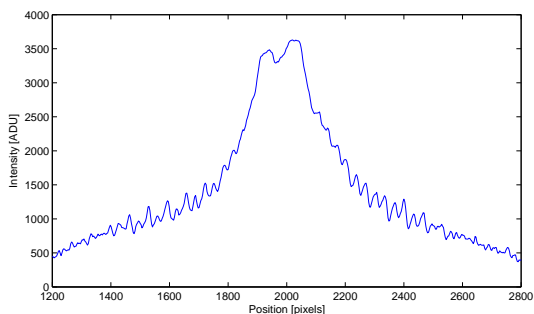

Figure 8.14: Graph of intensity from Fig. 8.13

The resolution was also tested experimentally with the two-hole apertures of the various hole distances. Resulting image for holes of angle distance 30' is shown on Fig. 8.17. Graph of intensity along the horisontal axis is shown on Fig. 8.18. The minimal value of intensity between the main peaks is approx. 45% of intensity of the lower peak. Sources are well resolved.

Analogous results for angle distance 20' are shown on Fig. 8.19 and Fig. 8.20. The minimal value of intensity between the main peaks is approx. 69% of intensity of the lower peak. Sources are resolved.

Analogous results for angle distance 10' are shown on Fig. 8.21 and Fig. 8.22. Sources are not resolved.

8.2.3   Assesments

For the intended use in a space all-sky monitor, the angular resolution must be in the order of tens of arcus minutes or better. If it will, the lobster eye
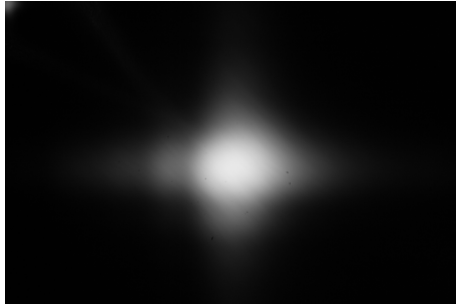
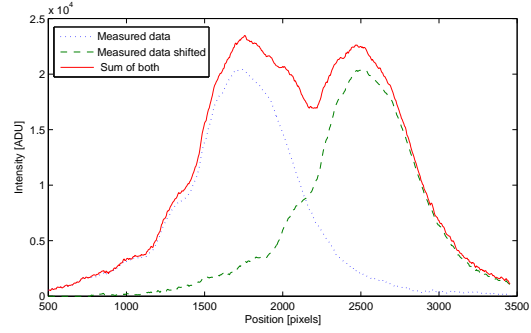Figure 8.15: Image from XTM-90 with single aperture

Figure 8.16: Estimation of spatial resolution of XTM-90 in horizontal axis

Figure 8.17: Image from XTM-90 with two-hole aperture with angle distance 30'
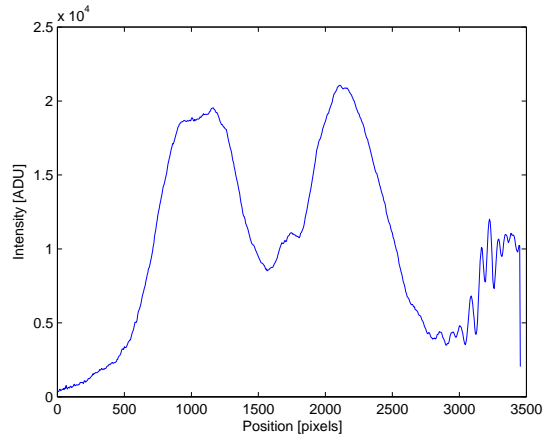
Figure 8.18: Graph of intensity from Fig. 8.17

telescope can estimate the X-ray source position with the sufficient accuracy for a larger telescope, which can analyse the source in detail. Tests in visible light shows this goal is reachable.

For the module XTM-25 with the lobster eye P-25, test with a single aperture gives estimation of angular resolution as 16'. FWHM resolution is 17'. Tests with two-hole appertures (aligned in the axis of one system of mirrors) confirm the value between $10' - 20'$. Theoretical value of the angular resolution calculated using the equation(4.6) reaches 5.5'.

For the module XTM-90 with lobster eye P-90, test with a single aperture gives estimation of angular resolution as 19'. The FWHM resolution is slightly better, it reaches 17'. Tests with two-hole appertures (aligned in

Figure 8.19: Image from XTM-90 with two-hole aperture with angle distance 20'
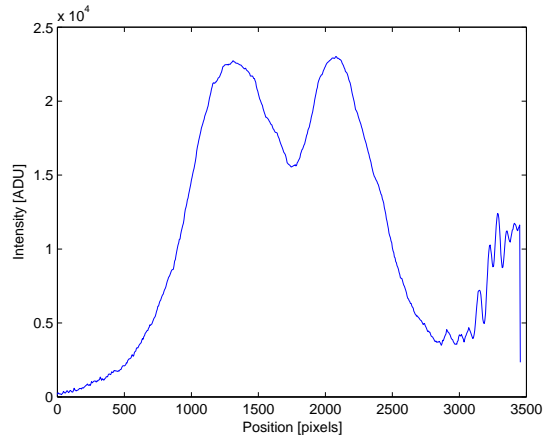
Figure 8.20: Graph of intensity from Fig. 8.11

the axis of one system of mirrors) confirm the value between $10' - 20'$. Theoretical value of the angular resolution calculated using the equation(4.6) reaches $1.5'$.

As explained above, it can be expected that spatial resolution in X-ray will be even slightly bettet give better results than in visible light.

Figure 8.21: Image from XTM-90 with two-hole aperture with angle distance 10'

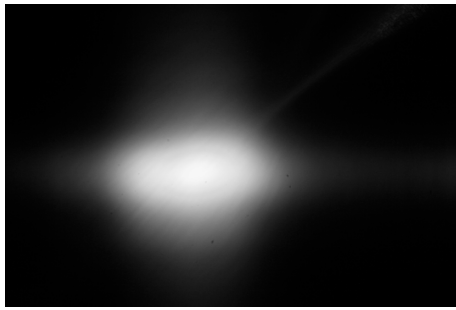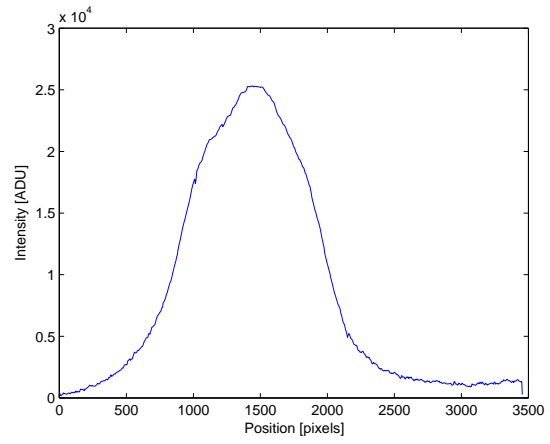Figure 8.22: Graph of intensity from Fig. 8.13

59

8.3 Test of lobster eye P-25 in X-ray beam XACT

For the imaging tests of the lobster eye optics designed for imaging from infinity, the complex laboratory equipment is necessary. X-ray source must generate a parallel (or almost parallel) X-ray beam. Width of this beam must be sufficient to illuminate whole active area of the optics. The experimental equipment also must contain the X-ray image detector. The detector as well as tested optics must be placed on remotely controlled positioning devices. In the Europe, suited test facilities are placed in Max Planck Institute (Germany), in University of Palermo (Italy) and in University of Leicester (Great Britain).

The collaboration was established with the National Institute for Astrophysics of Univsersity of Palermo (INAF-OAPA). Here, the performance of the lobster eye P-25 (see Tab. 6.1) was experimentally tested in quasi-parallel-beam, full-imaging mode using the 35 meters long X-ray beamline XACT (X-ray Astronomy Calibration and Testing Facility) [6, 43], see Fig. 8.23-Fig. 8.25. As the detector, a microchannel plate (MCP) also provided by INAF-OAPA was used. We kindly thank this institution for providing its equipment. We would like to thank namely to Prof. Alfonso Collura, Dr. Marco Barbera and Dr. Salvatore Varisco. Note that imaging tests in quasi-parallel beam with Schmidt LE optics of used size have never been published previously.

8.3.1 Experimental setup

The X-ray tube source with an exchangeable target and exchangeable transmission filters is permanently installed at one side of the tunnel. Used energy lines, corresponding acceleration voltage, targets and filters are listed in Tab. 8.1.

Energy [keV]	target material	filter material	filter thickness [μm]	acceleration voltage [kV]
0.28	carbon	polypropylen+copper	1+0.5	2.5
0.93	copper	polypropylen+copper	1+0.5	2.5
1.5	aluminium	aluminium	10	5.5
2.9	silver	silver	3	5.5
4.5	titanium	titanium	20	8.0
8.0	copper	copper	20	12.5

Table 8.1: Energy lines used in X-ray beam in INAF-OAPA

Figure 8.23: Vacuum X-ray tunnel XACT at INAF-OAPA, Palermo

Energy lines in Tab. 8.1 have been selected as follows. Line 0.93keV was the nearest to the optimal energy for lobster eye P-25 (which is 1keV) from the available lines. Also, from the available lines, one near lower (0.28keV) and one near higher lines (1.5keV) have been selected. Line 4.5keV was chosen, because it is the optimal energy for LE with Medipix2 in space, as explained in chapter 5.1.1. Also, from the available lines, one near lower (2.9keV) and one near higher line (8.0keV) have been chosen.

Tested lobster eye P-25 was placed on the oposite side of the tunnel on a device allowing remotely controlled rotations around vertical and horisontal axes perpendicular to the beam axis. The detector was placed on a device allowing remotely controlled translation in all basic three directions. The experimental arrangement of LE, MCP and positioning devices can be seen on Fig. 8.26. Because the target was small (less than 1cm) at large distance (35m), angle size of the source is less than 1 arcmin. Theoretical value of angle resolution of the used LE is 5.5arcmin, true value can not be better. For these reasons, the used source can be considered as a good aproximation of a point source in the infinity.

Figure 8.24: Control room of XACT

8.3.2 Centering the optics, estimation of field of view and basic images

First, the limiting positions, when one arm of the cross vanishes have been found, see Fig. 8.27. The field of view ϕ defined by these position in both axes can be estimated as

$$\phi = \mathbf{2.9}° \pm \mathbf{0.2}° \tag{8.1}$$

Note that these measurements have been performed at energy 1.5keV. Note results for all energy lines listed in Tab. 8.1 excepting the line 8keV leaded to the same value. Theoretical value calculated using the relation (4.11) is 2.7°. This value corresponds to the measured one. At the line 8keV, it was impossible to find these positions, because limiting angle of gold at 8keV is only approx. 0.5′ and for this reason, used lobster eye does not operate in the mentioned corner position at 8keV.

For the further experiments, the middle value between values specified on Fig. 8.27, i.e. pitch $= -1.25°$, yaw $= 0.05°$ was considered as the central position of the optics.

For all energy lines listed in Tab. 8.1, the images at central position of the optics were obtained. These results are shown on Fig. 8.28. In these pictures, it is seen that the detector is circular and some cells near the border produce

Figure 8.25: Door of the test chamber of XACT in the clean room

major level of noise.

8.3.3 Angular resolution

At all energies, FWHM of the central peak corresponds to the angle of view within the interval $12 - 13'$. This value represents one possible method of estimating the angular resolution.

Another mothod of estimation of the angular resolution is based on summing the profile of focal cross along one line with the same data shifted, to simulate resulting image of two point sources. Searching for position, when intensity between peaks of the sum falls to 80% of intensity of lower peak (as it was done in section 8.2) the value $13 \pm 1'$ was estimated as the spatial resolution for all used energy lines. This value corresponds to the FWHM
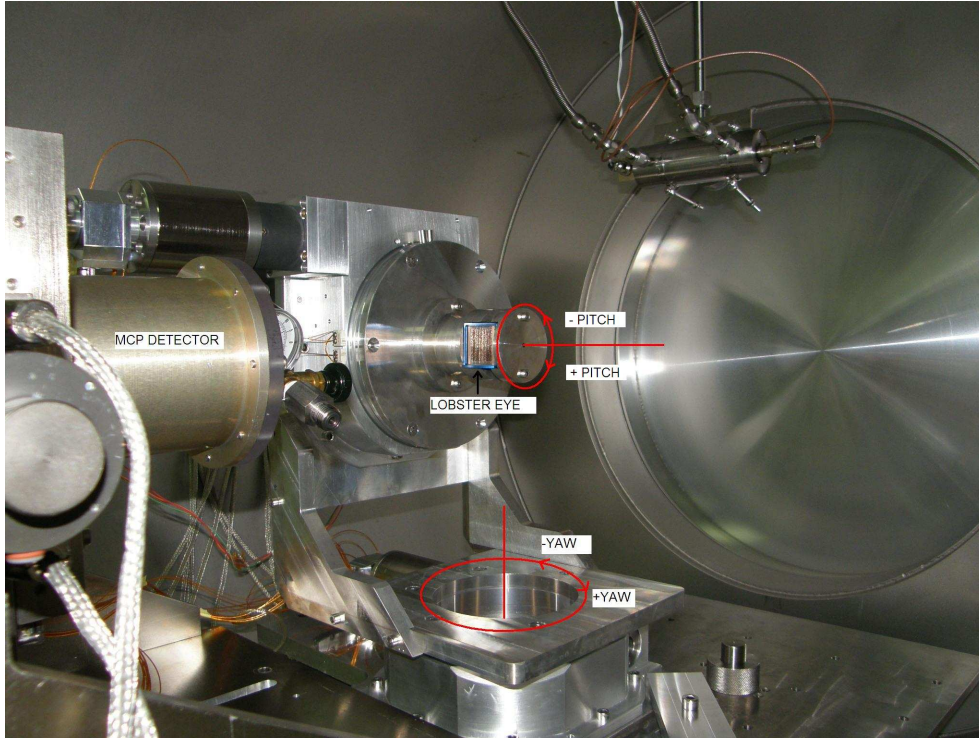
Figure 8.26: Lobster eye and detector on positioning devices in the test chamber

spatial resolution. The corresponding graph for energy of 930eV is shown on Fig. 8.29. Graphs for the other used energies are similar.

As it was expected, the obtained angular resolution of approx. 13′ in X-rays is better than the value 16′ in visible light (see chapter 8.2.2), however, it is still essentially worse than the theoretical value 5.5′.

It means, the focus is smudged. This fact also can be seen on the Fig. 8.30, where the experimental image on the energy 930eV is compared with the result of simulation.

8.3.4 Estimation of Gain

Gain was estimated as the ratio between the average flux in the main spot and flux of the incoming X-ray. Here, the square of size $300\mu m$ (i.e. projection of the central chamber) with maximal total flux was considered as the main spot. The results are listed in Tab. 8.2, they are compared to the results of simulations (see chapter 7). Comparsion of experimentally obtained values of the gain with the results of the simulations is also given on Fig. 8.31.

Energy [keV]	measured gain	simulated gain
0.28	78 ± 2	820
0.93	64 ± 1	764
1.5	75 ± 1	786
2.9	26 ± 1	318
4.5	27 ± 1	262
8.0	11 ± 1	78

Table 8.2: Gain of P-25 at various energies

Measured values are approximately 10 times smaller than the simulated ones.

8.3.5 Gain as function of incident beam angle

At three selected lines: 0.28keV, 0.93keV and 4.5keV the gain was measured as a function of incident beam angle. In these measurements, optics was focused and pitch angle was fixed. Yaw angle is the incident beam angle. Results are shown on Fig. 8.32-Fig. 8.34.

8.4 Assesments

Tests of the lobster eye P-25 in the XACT facility represent the most important experimental part of the work. Results show that the capability of the lobster eye P-25 is many times worse than it has been expected by theoretical considerations. Nevertheless, the lobster eye P-25 is still well capable to be implemented into an experimental space lobster eye X-ray telescope.

Measured angular resolution reaches $13'$, this value is more than two times worse than the theoretical value $5.5'$. Nevertheless, this value is adequate for an all-sky monitor searching for X-ray transients to be analysed by subsequent narrow field instrument.

The measured gain is approx. 10 times worse than the gain obtained by simulations. It means, the telescope will have 10 times worse sensitivity than expected.

Both facts, worse angular resolution and gain, can be clarified by two facts related to the manufacturing process. At first, mirrors have not been located to the ideal positions. It causes smudging of the image and decrease in gain. The manufacturer, Rigaku Innovative Technologies Europe, s.r.o.(former Reflex, s.r.o.) gave me information of the reached accuracy of the settling of the

mirrors. The root of mean square error of the deviation of the mirror spacing is approx. 2.5μm. This error has the cumulative character, i.e. if one mirror is settled with some deviation, the following mirror is settled with the same deviation plus the deviation of its own settling. In the simulation program, these deviations were simulated. The resulting gain was decreased two- to five-times. Second key manufacturing challenge is the flatness of the mirrors. Sure, mirrors are never ideally flat and their deflections casuses decreasing of the gain. The deflection of the mirrors reaches the order of the tens of microns. However, this fact cannot be simulated by the program using the presented algorithm and the exact proof that this fact cause the decrease of the gain will be the subject of further research. Partially, the lower measured values of the gain are also caused by the fact, that the central position found as the center between the corner position is not the position of the maximal gain as seen on the Fig. 8.32-Fig. 8.34. This fact is also given by the mentioned manufacturing deviations.

The experiment also showed the lobster eye P-25 cannot be effectivelly used with the Medipix2/Timepix detectors. On the graph Fig. 8.31 it is seen the gain rapidly decreases above the energy of approx. 2keV due to M_{a1} absorption line of gold. This absorption line lays at the energy 2.1keV [39]. However, the Midipix2/Timepix detectors are usable only for detection of photons of energies above approx. 3.5keV.
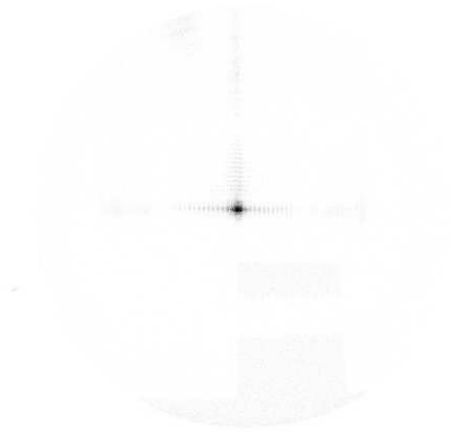
(a) pitch $= +0.2°$
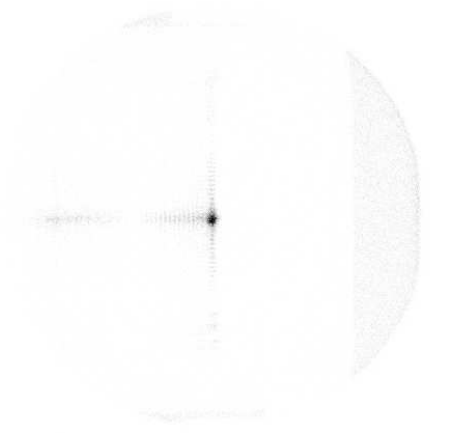
(b) pitch $= -2.7°$
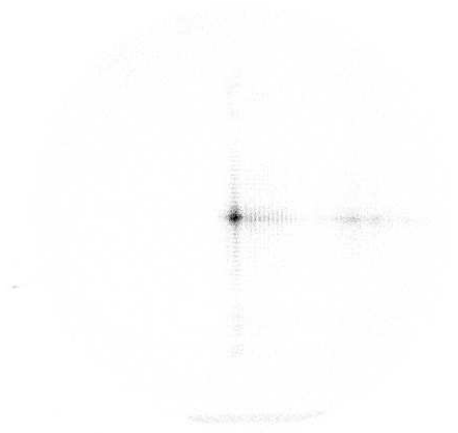
(c) yaw $= +1.5°$

(d) yaw $= -1.4°$

Figure 8.27: Corner positions of P-25
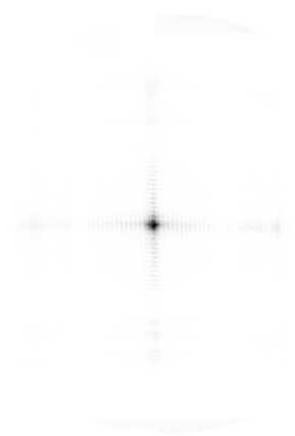
(a) 0.28keV
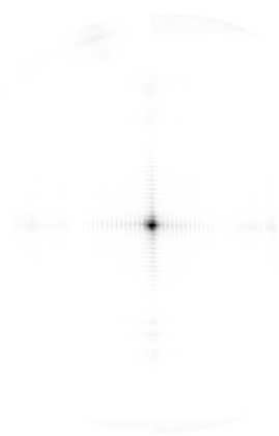
(b) 0.93keV
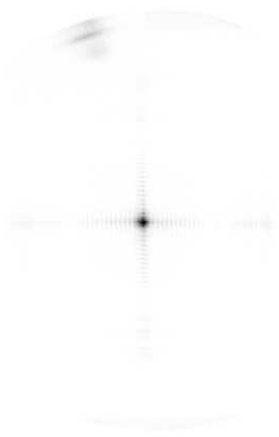
(c) 1.5keV
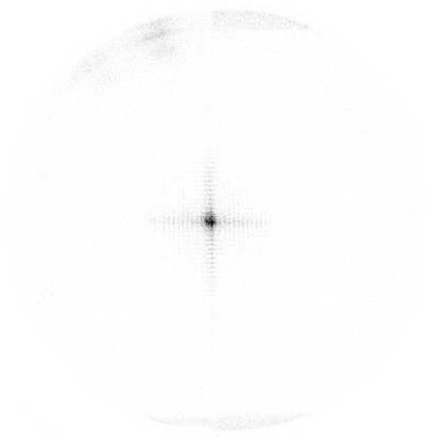
(d) 2.9keV
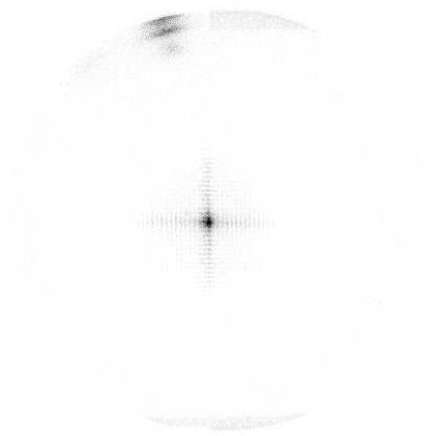
(e) 4.5keV
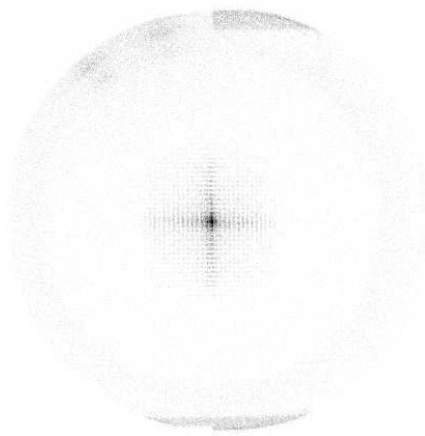
(f) 8.0keV

Figure 8.28: Basic images obtained by P-25 for various energies
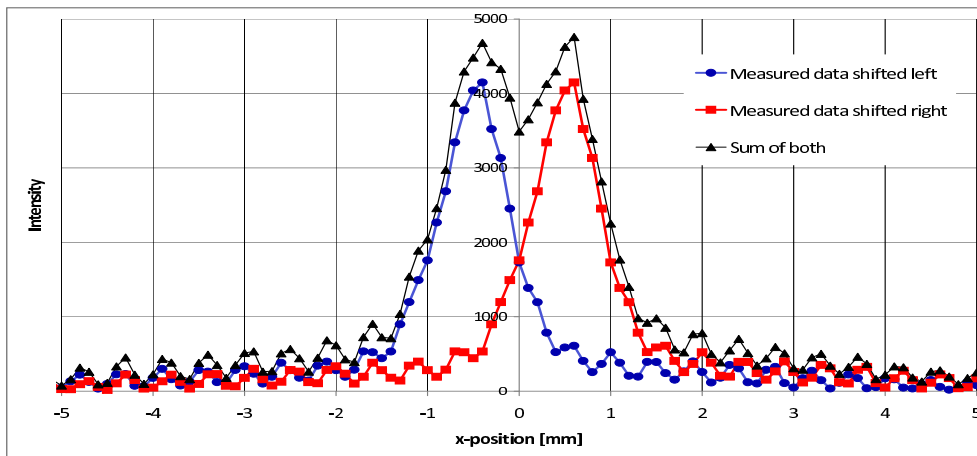
Figure 8.29: Estimation of angular resolution of P-25 at energy 930eV

(a) Experiment
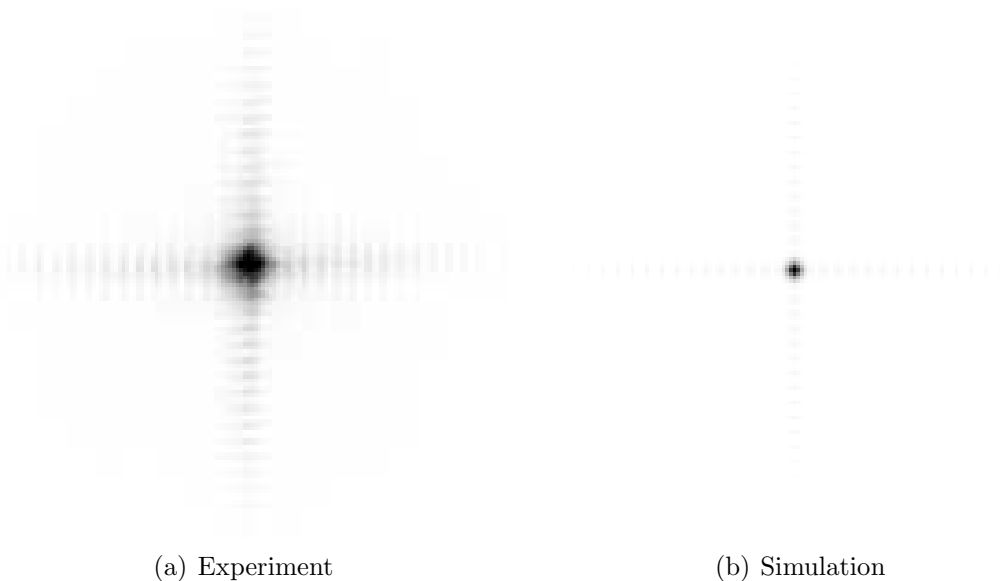
(b) Simulation

Figure 8.30: Comparsion of the experimentally obtined focal cross with results of simulation for lobster eye P-25 at energy 930eV. Both images are of the same scale.

(a) Experiment   (b) Simulation
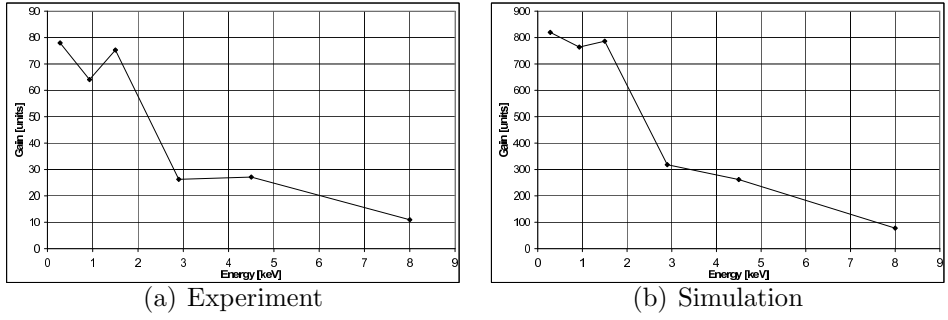
Figure 8.31: Gain of lobster eye P-25 at various energies
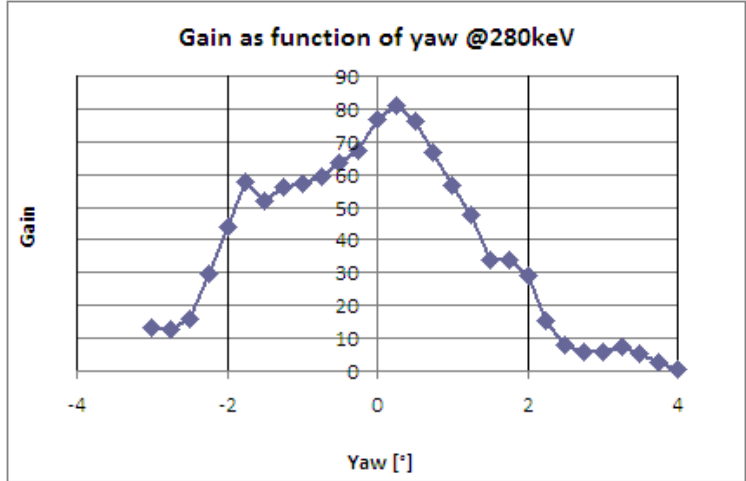
Figure 8.32: Gain as function of incident beam angle at energy 280eV
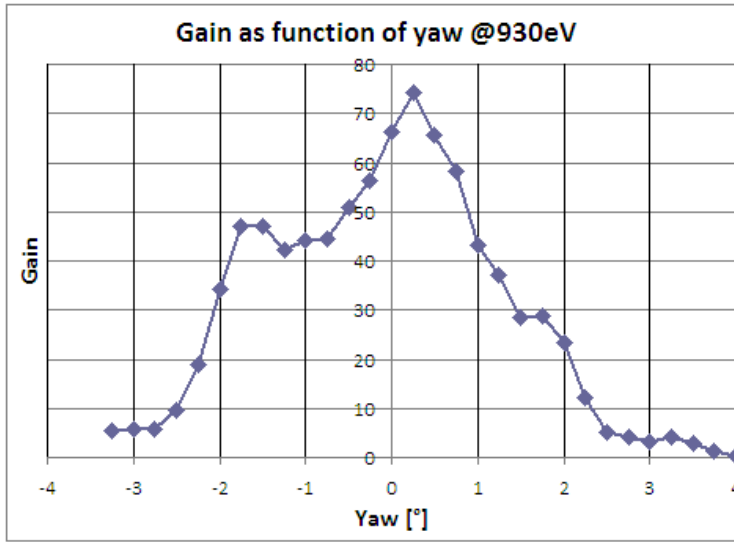
Figure 8.33: Gain as function of incident beam angle at energy 0.93keV
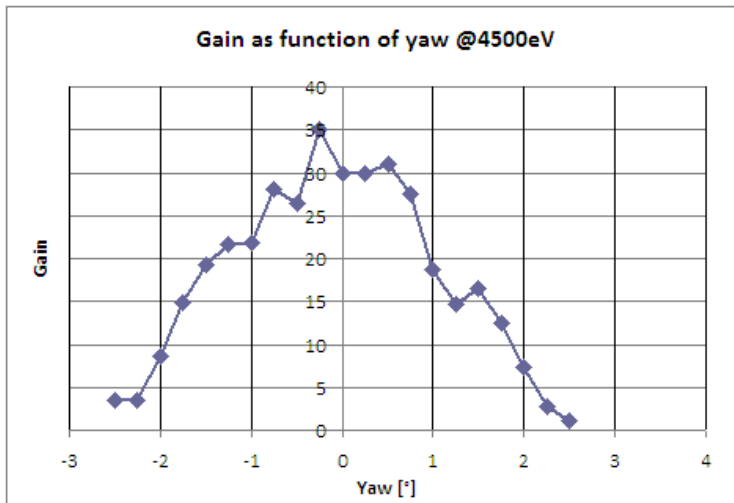
Figure 8.34: Gain as function of incident beam angle at energy 4.5keV

Chapter 9

Conclusions

All goals of the work have been achieved. Medipix2 and Timepix devices were tested. Basic tests of imaging from finite distance by lobster eye were performed. Two experimental modules called XTM-25 and XTM-90 with two different pieces of lobster eyes called P-25 and P-90 were built. Both these modules were tested in visible light, standalone lobster eye P-25 was tested also in X-rays. A related simulation program was created.

Medipix2 and Timepix devices were proven to be suitable as detectors for the lobster eyes designed for the energies above approx. 3.5keV. At the energy 8keV, this fact has been shown experimentally. At this energy, used lobster eye for imaging from finite distance was operative, it shows relatively large field of view and moderate yet sufficient angular resolution.

Tests in visible light of both lobster eyes P-25 and P-90 for imaging from infinite distance also showed the both lobster eyes are operative and they have adequate angular resolution.

Tests of lobster eye P-25 in X-rays proved the lobster eye P-25 has large field of view and adequate angular resolution. Measured field of view corresponds to theory, however measured angular resolution is approx. $2-3$ times worse than results of simulations. Also, gain (amplification of the flux) at several energy lines was measured. Measured gain is approx. 10 times worse than gain estimated by simulations. These differences can be attributed to manufacturing deviations. Tests revealed that current manufacturing accuracy is not sufficient for building small lobster eyes with high gain and high spatial resolution.

Although P-25 has worse properties than it is estimated by simulation, it can still be used in a small satellite for technological and proof-of-concept test. Tests showed the Medipix2 and Timepix devices are not suitable detectors for this lobster eye. The Medipix2 or Timepix device can be used jointly with lobster eye P-90. Though, this lobster eye has larger focal length and

small field of view for the intended application - cubesat X-ray wide-field-of-view monitor.

To sum up, results indicate that a small experimental lobster eye telescope for proving of the technology in the space is realisable.

Chapter 10

Future work

For the future, it is planned tu build a follow-up prototype of X-ray telescope, completely designed for a space experiment.

As a good platform for future application in space, a satellite of the type CubeSat type seems most feasible and appropriate. These satellites have the basic outer dimensions of $100 \times 100 \times 100$mm and their mass has to be less than 1kg. Their basic diameter can be multiplied by 1, 1.5, 2 or 3. By the same factor, the mass limit is increased. This allows to build a satellite of the outer dimensions of $300 \times 100 \times 100$mm with maximal mass of 3kg.

This allows to use the lobter eye P-25 which has focal length of 250mm and it is designed for optimal efficiency at energy 1keV. In this case, the Medipix2/Timepix are not suitable detecting devices, because they detect energies above approx 3.5keV. As well, using another semiconductor detector represents a complex problem, because they require to be cooled in order to detect energies about 1keV. So a two- or three-staged MCP can be a good choice. These devices operate at wide scale of temperatures, they are radiation durable. The resolution around 100μm has been proven to be sufficient for using with the lobster eye P-25. They provide less detection efficiency should not be an obstacle in the first flight experiment.

The usual trajectory of CubeSats is roughly circle at the altitude 600-800km with a big inclination around 88°. This big inclination ensures the stable ratio between time of illumination by sun and time in the Earth shade. It is an useful factor for power supply systems design. Also, this stable ratio alows to use only passive temperature stabilisation, which can ensure variation of the temperature inside a satellite within the interval $10 - 50$°C. At these temperatures, usual electronic components operate. Trajectory of CubeSats drifts by 1° per day. Hence, if the lobster eye will fly with its optical axis stabilised perpendiculary to the Earth surface, it can scan the whole sky per year.

Chapter 11

Fulfillment of goals

11.1 Medipix2 and Timepix

Spectroscopic properties of Medipix2 and Timepix devices were tested. Results are given in section 5.1.1. In the same section, other properties of Medipix2 and Timepix devices acquired from the cited literature are given.

11.2 Tests of lobster eye optics for X-ray imaging from finite distance

Basic tests of imaging from finite distance by lobster eye were performed with the lobster eye specimen L.U.N.D. Its field of view and spatial resolution were determined. Image distortion as function of source position was estimated and compared with simulations. Results are given in section 8.1.

11.3 Experimental modules

Two experimental modules called XTM-25 and XTM-90 with two different pieces of lobster eyes called P-25 and P-90 were built. These modules are introduced in chapter 6. Both these modules were tested in visible light, Results are presented in section 8.2.

11.4 Tests of lobster eye optics for X-ray imaging from infinite distance

To reach this goal, the collaboration between DCE FEE CTU and National Institute for Astrophysics of University of Palermo (Italy) was established. This institute kindly provided its facility XACT for this experiment. Here, the lobster eye P-25 was tested in X-rays at various energies from 280eV to 8keV. Its field of view, gain and spatial resolution were determined. At chosen lines, gain as the function of the source position was measured. Results are shown in section 8.3.

11.5 Simulation program

A related simulation program was created. The program simulates lobster eye operation in the centered arrangement (i.e. when the X-ray source and the detector lay in the optical axes of the lobster eye). This program can simulate behavior of any lobster eye configuration for any energy, visualize the image and estimate the gain. The program is introduced in chapter 7.

11.6 Assesment

Each result is assessed in the corresponding section. General assessment is given in conclusions.

Author's SCI and SCI-expanded publications

[S1] V. Tichý, M. Hromčík, R. Hudec, A. Inneman, J. Maršík, V. Maršíková, L. Pína, Tests of Lobster-Eye Optics for a Small X-Ray Telescope, Balt. Astr. 18 (2009) 362-368

[S2] V. Tichý, L. Švéda, J. Maršík, J. Jakůbek, V. Maršíková, L. Pína, R. Hudec, M. Hromčík, Tests of Imaging with Lobster Eye X-Ray Optics and Medipix2 Detector, Balt. Astr. 18 (2009) 369-373

[S3] V. Tichý, M. Barbera, A. Collura, M. Hromčík, R. Hudec, A. Inneman, J. Jakůbek, J. Maršík, L. Pína, V. Maršíková, L. Pína, S. Varisco, Tests of Lobster Eye Optics for Small Space X-ray Telescope, accepted in Nucl. Instr. Meth. A (2010), available on-line at http://dx.doi.org/10.1016/j.nima.2010.06.157

[S4] J. Jakůbek, J. Dammer, T. Holý, M. Jakůbek, S. Pospíšil, V. Tichý, J. Uher, D. Vavřík: Spectrometric Properties of TimePix Detector for X-ray Color and Phase Sensitive Radiography, IEEE NSS Conf. Proc. (2007) N50-6

[S5] V. Tichý, T. Holý, J. Jakůbek, V. Linhart, S. Pospísil, Z. Vykydal: X-Ray Fluorescence Imaging with Pixel Detectors, Nucl. Inst. Meth. A 591 (2008) 67-70

[S6] M. Platkevič, V. Bočarov, J. Jakůbek, S. Pospísil, V. Tichý, Z. Vykydal: Signal Processor controlled USB 2.0 Interface for Medipix2 Detector, Nucl. Inst. Meth. A 591 (2008) 245-247

[S7] J. Žemlička, J. Jakůbek, M. Kroupa, V. Tichý: Energy and Position Sensitive Pixel Detector Timepix for X-Ray Fluorescence Imaging, Nucl. Inst. Meth. A 607 (2009) 202-204

Author's publications in conference proceedings and conference presentations

[P1] V. Tichý, L. Švéda, J. Maršík, J. Jakůbek, V. Semencová, L. Pína, R. Hudec, M. Hromčík: Capabilities of Medipix2 and Timepix Devices as Detectors for Lobster Eye X-Ray Optics, poster presentation and paper in proceedings of International Conference on Space Optics, Toulouse, France, October 14-17

[P2] V. Tichý, M. Hromčík, R. Hudec, A. Inneman, J. Jakůbek, J. Maršík, L. Pína, V. Semencová, L. Švéda: Small x-ray telescope based on lobster eye x-ray optics and pixel detector, oral presentation at SPIE Europe Optics + Optoelectronics Conference, Prague, Czech Republic, April 20-23, 2009, paper in Proc. SPIE, Vol. 7360, 736011

[P3] D. Vavřík, T. Holý, J. Jakůbek, J. Bryscejn, V. Tichý, Z. Vykydal, J. Valach, oral presentation and paper in proceedings of Radiographic Observation of Damage Zone Evolution in High Ductile Specimen, 16th European Conference of Fracture, Alexandroupolis, Greece, July 3-7, 2006

[P4] L. Švéda, V. Tichý, J. Maršík, J. Jakůbek, V. Semencová, R. Hudec, M. Hromčík, L. Pína: Zobrazovací vlastnosti rentgenové optiky račí oko - srovnání teorie a experimentu, Technical Computing Prague Conf. Proc. (2008)

[P5] V. Tichý, M. Hromčík, R. Hudec, A. Inneman, J. Jakůbek, J. Maršík, L. Pína, V. Semencová, L. Pína, L. Švéda, Idea of Small Space X-Ray Telescope Based on Lobter Eye Optics and Medipix2 Detector, oral presentation at 6th INTEGRAL/BART International Workshop, Karlsbad, Czech Republic, March 26-29, 2009

[P6] V. Tichý, L. Švéda, J. Maršík, J. Jakůbek, V. Semencová, L. Pína, R. Hudec, M. Hromčík: Capabilities of Medipix2 and Timepix Devices as Detectors for Lobster Eye X-Ray Optics, poster presentation at International Workshop on Astronomical XRay Optics, Prague, Czech Republic, December 2-6, 2008

[P7] V. Tichý, M. Barbera, A. Collura, M. Hromčík, R. Hudec, A. Inneman, J. Maršík, L. Pína, V. Maršíková, S. Varisco, Tests of Lobster Eye Optics for Possible Space Mission, poster presentation at International Workshop on Astronomical XRay Optics, Prague, Czech Republic, December 6-9, 2009

[P8] V. Tichý, M. Barbera, A. Collura, M. Hromčík, R. Hudec, A. Inneman, J. Jakůbek, J. Maršík, L. Pína, V. Maršíková, L. Pína, S. Varisco, Lobster Eye as Optics for Small Space X-ray Telescope, poster presentation at 11th International Workshop on Radiation Imaging Detectors, Prague, Czech Republic, June 28-July 2, 2009

[P9] V. Tichý, M. Barbera, A. Collura, M. Hromčík, R. Hudec, A. Inneman, J. Jakůbek, J. Maršík, L. Pína, V. Maršíková, L. Pína, S. Varisco, Lobster Eye as Optics for Small Space X-ray Telescope, poster presentation at Swift Mission Conference Celebrating 5 Years, State College, Pennsylvania, USA, November 17-20, 2009

[P10] V. Tichý, L. Švéda, J. Maršík, J. Jakůbek, V. Semencová, L. Pína, R. Hudec, M. Hromčík, Capabilities of Medipix2 and Timepix Devices as Detectors for Lobster Eye X-Ray Optics, poster presentation at 6th INTEGRAL/BART International Workshop, Karlsbad, Czech Republic, March 26-29, 2009

[P11] V. Tichý, M. Barbera, A. Collura, M. Hromčík, R. Hudec, A. Inneman, J. Maršík, L. Pína, V. Maršíková, S. Varisco, Tests of Lobster Eye Optics for Possible Space Mission, poster presentation at 7th INTEGRAL/BART International Workshop, Karlsbad, Czech Republic, April 14-18, 2010

[P12] V. Tichý, Small X-Ray Telescope Based on Lobster Eye Optics and Pixel Detector, poster presentation and paper in proceedings of 13th International Student Conference on Electrical Engineering "Poster", Prague, Czech Republic, May 21, 2009

[P13] V. Tichý, M. Hromčík, J. Jakůbek, Applications of the Medipix Type Detectors Combined with X-Ray Optics poster presentation and paper

in proceedings of 18th Annual CTU University-Wide Seminar "Workshop", Prague, Czech Republic, February 16-20, 2009

Author's presentations in public media

[M1] interview within the article České račí oko poletí do kosmu, Lidové noviny, January 12 (2010), page 29

[M2] interview for Czech radio, broadcasted in April 15, 2010, available at http://www.rozhlas.cz/mozaika/veda/

Literature

[1] J. R. P. Angel: Lobster eyes as X-ray telescopes, ApJ 233, 364-373, October 1979

[2] Aschenbach, Bernd, Design, construction, and performance of the Rosat high-resolution X-ray mirror assembly, Proc. SPIE 27 (1988) 1404-1413

[3] G. Boella et al., BeppoSAX, The wide band mission for X-ray astronomy, A&AS 122 (1997) 299-307

[4] M. Born, E. Wolf, Principles of optics: electromagnetic theory of propagation, interference and diffraction of light, Cambridge University Press, Cambridge 1997

[5] W. B. Colson, J. McPherson and F. T. King, Rev. Sci. Instr. 44 (1973) 1694

[6] A. Collura, M. Barbera, G. Inzerillo, F. Mirabello, S. Sciortino, S. Serio, Proc. SPIE (1994) 2280, 206

[7] A. C. Edge, G. C. Stewart, G. C., EXOSAT observations of clusters of galaxies. I - The X-ray data. II - X-ray to optical correlations, MNRAS 252 (1991) 414-441

[8] J. H. Hubbel, S. M. Seltzer: Tables of X-Ray Mass Attenuation Coefficients and Mass Energy Absorption Coefficients, available online at http://physics.nist.gov/PhysRefData/XrayMassCoef/cover.html

[9] R. Hudec, A. Inneman, L. Pina, V. Hudcova, L. Sveda, H. Ticha: Lobster eye x-ray telescopes: recent progress, Proceedings of SPIE, vol. 4851 (2003) 578-4851

[10] A. Inneman: Technologické aspekty vývoje a výroby optických prvků pro rentgenové záření, PhD. thesis, Czech Technical University in Prague, Faculty of Mechanical Engineering, 2001

[11] J. Jakůbek, Energy Sensitive X-ray Radiography and Charge Sharing Effect in Pixelated Detector, Nucl. Inst. Meth. A 607 (2009) 192-195

[12] F. Jansen et al., XMM-Newton observatory. I. The spacecraft and operations A&A 365 (2001) L1-L6

[13] P. Kahabka, E. P. J. van den Heuvel, Luminous Supersoft X-Ray Sources, ApJ Annual Review 35 (1997) 69-100

[14] E. Kellogg et al., The X-Ray Structure of the VELA X Region Observed from UHURU, ApJ 183 (1973) 935-940

[15] P. Kirkpatrick and A. V. Baez, Formation of optical images by X-rays, J. Opt. Soc. Am. 38 (1948) 766

[16] M. Kirsch et al., Crab: the standard x-ray candle with all (modern) x-ray satellites Proc. SPIE, 5898 (2005) 22-33

[17] P. A. J. de Korte et al., The X-ray imaging telescopes on EXOSAT, Space Science Reviews 30 (1981) 495-511

[18] S. M. Lea, R. Mushotzky, S. S. Holt, Einstein Observatory solid state spectrometer observations of M87 and the Virgo cluster, ApJ 262 (1982) 24-32

[19] X. Llopart, M. Campbell, R. Dinapoli, D. San Segundo, E. Pernigotti: Medipix2, a 64k Pixel Readout with $55\mu m$ Square Elements Working in Single Photon Counting Mode, IEEE Trans. Nucl. Sci., 49:2279-2283 (2001)

[20] X. Llopart, R. Ballabriga, M. Campbell, L. Tlustos, W. Wong, Timepix, a 65k Programmable Pixel Readout Chip for Arrival Time, Energy and/or Photon Counting Measurements, Nucl. Instr. Meth. A, 581 (2007) 485-494

[21] K. Mason et al., The XMM-Newton optical/UV monitor telescope, A&A 365 (2001) L36-L44

[22] N. Meidinger et al.: Next generation of pnCCDs for X-ray spectroscopy and imaging, NIM A 568 (2006) 141-148

[23] B. Mikulec: Single Photon Detection with Semiconductor Pixel Arrays for Medicial Imaging Applications, PhD. thesis, University of Vienna, Austria 2000

[24] E. Pfeffermann et al., The focal plane instrumentation of the ROSAT telescope, Proc. SPIE 733 (1987) 519

[25] C. Ponchut: Correction of the Charge Sharing in Photon-Counting Pixel Detector Data, Nucl. Inst. Meth. A, 591 (2008) 311-313

[26] W. H. K. Schmidt: A proposed X-ray focusing device with wide field of view for use in X-ray astronomy, Nucl. Instr. And Methods 127, 285-292, 1975

[27] E. J. Schreier, G. Fabbiano, Recent UHURU results on Centaurus X-3, NASSP 589 (1976) 197-206

[28] L. Strüder et al., The European Photon Imaging Camera on XMM-Newton: The pn-CCD camera, A&A 365 (2001) L18-26

[29] L. Švéda, Multi-Foil X-Ray Optical Systems and Image Analysis in High-Temperature Plasma Physics, PhD. thesis, Faculty of Nuclear Sciences and Physical Engineering, Czech Technical University in Prague, 2006

[30] H. Tananbaum et al., Discovery of a Periodic Pulsating Binary X-Ray Source in Hercules from UHURU, ApJ 174 (1972) L143

[31] J. Truemper, The ROSAT mission, AdSpR 2 (1982) 241-249

[32] M. J. L. Turner et al., The European Photon Imaging Camera on XMM-Newton: The MOS cameras, A&A 365 (2001) L27-L35

[33] T. J. Turner, K. A. Pounds, The EXOSAT spectral survey of AGN, MNRAS 240 (1989) 833-880

[34] H. Wolter: A Generalized Schwarzschild Mirror. Systems For Use at Glancing Incidence for X-ray Imaging, Ann. Physik. 10 (1952) 286

[35] J. L. Wiza: MICROCHANNEL PLATE DETECTORS, Nucl. Inst. Meth. 162 (1979) 587-601

[36] Dev-C++, http://www.bloodshed.net/dev/devcpp.html

[37] Wikipedia, the free encyclopedia, http://www.wikipedia.org

[38] http://en.wikipedia.org/wiki/Fwhm

[39] http://henke.lbl.gov/optical_constants/

[40] http://www.elya.cz/en/xkioo2

[41] http://www-cxro.lbl.gov/

[42] http://altamira.asu.cas.cz

[43] http://www.astropa.unipa.it/XACT/index.html

[44] http://en.wikipedia.org/wiki/IEEE_754-1985

[45] http://www.elya.cz/cs/xann3d-free-edition

[46] http://heasarc.gsfc.nasa.gov/docs/einstein/heao2.html

[47] http://sci.esa.int/science-e/www/area/index.cfm?fareaid=32

[48] http://www.mpe.mpg.de/xray/wave/rosat/index.php?lang=en

[49] http://heasarc.gsfc.nasa.gov/docs/rosat/

[50] http://ledas-www.star.le.ac.uk/rosat-goc/

[51] http://ledas-www.star.le.ac.uk/info/user_guide/oldweb/node18.html

[52] http://heasarc.gsfc.nasa.gov/docs/rosat/wfc.html

[53] http://heasarc.gsfc.nasa.gov/docs/xte/XTE.html

[54] http://xte.mit.edu

[55] http://www.asdc.asi.it/bepposax/

[56] http://heasarc.gsfc.nasa.gov/docs/sax/saxgof.html

[57] http://www.asdc.asi.it/bepposax/wfc.html

[58] http://www.nasa.gov/centers/marshall/news/background/facts/cxoquick.html

[59] http://www.nasa.gov/mission_pages/chandra/main/index.html

[60] http://www.astro.psu.edu/xray/axaf/acis.html

[61] http://asc.harvard.edu/cdo/about_chandra/

[62] http://chandra.harvard.edu

[63] http://chandra.harvard.edu/about/science_instruments.html

[64] http://xmm.esac.esa.int

[65] http://xmm.sonoma.edu

[66] http://solarsystem.nasa.gov/missions/profile.cfm?MCode=XMM

[67] http://xmm.esac.esa.int/external/xmm_user_support
/documentation/technical/Mirrors/index.shtml

[68] http://www.cubesat.com

[69] http://www.cubesat.org

[70] http://www.esa.org

[71] http://www.spacemaster.eu

[72] http://www.utef.cvut.cz

[73] http://www.astropa.unipa.it

[74] http://www.rigaku.com

[75] http://pmo.fs.cvut.cz/wiki/index.php?title=Hlavní_strana

[76] http://heasarc.gsfc.nasa.gov/docs/uhuru/uhuru.html